The Repertoire of Serous Ovarian Cancer Non-genetic Heterogeneity Revealed by Single-Cell Sequencing of Normal Fallopian Tube Epithelial Cells

DOI:
10.1016/j.ccell.2020.01.003

Document Version
Accepted author manuscript

The repertoire of serous ovarian cancer non-genetic heterogeneity revealed by single-cell sequencing of normal fallopian tube epithelial cells

Zhiyuan Hu, [1,2,3] Mara Artibani, [1,2,4,15] Abdulkhaliq Alsaadi, [1,2,15] Nina Wietek, [1,2,5] Matteo Morotti, [1,2,5] Tingyan Shi, [1,2] Zhe Zhong, [1,2] Laura Santana Gonzalez, [1,2] Salma El-Sahhar, [1,2] Mohammad KaramiNejadRanjbar, [1,2] Garry Mallett, [1,2] Yun Feng, [3] Kenta Masuda, [1,2] Yiyan Zheng, [1,2] Kay Chong, [1,2] Stephen Damato, [6] Sunanda Dhar, [6] Leticia Campo, [7] Riccardo Garruto Campanile, [5] Hooman Soleymani majd, [5] Vikram Rai, [8] David Maldonado-Perez, [9,10] Stephanie Jones, [9] Vincenzo Cerundolo, [11] Tatjana Sauka-Spengler, [4] Christopher Yau [3,12,13,14,*] and Ahmed Ashour Ahmed [1,2,5,16,*]

[1] Ovarian Cancer Cell Laboratory, MRC Weatherall Institute of Molecular Medicine, University of Oxford, Oxford, OX3 9DS, UK

[2] Nuffield Department of Women's & Reproductive Health, University of Oxford, Oxford, OX3 9DU, UK

[3] Wellcome Centre for Human Genetics, Nuffield Department of Medicine, University of Oxford, Oxford, OX3 7BN, UK

[4] Gene Regulatory Networks in Development and Disease Laboratory, MRC Weatherall Institute of Molecular Medicine, Radcliffe Department of Medicine, University of Oxford, Oxford, OX3 9DS, UK

[5] Department of Gynecological Oncology, Churchill Hospital, Oxford University Hospitals, Oxford, OX3 7LE, UK

[6] Department of Histopathology, Oxford University Hospitals, Oxford, OX3 9DU, UK

[7] Department of Oncology, University of Oxford, Oxford, OX3 7DQ, UK

[8] Department of Gynaecology, Oxford University Hospitals NHS Trust, Oxford, OX3 9DU, UK

[9] Oxford Radcliffe Biobank, Nuffield Department of Surgical Sciences, University of Oxford, Oxford, OX3 9DU, UK

[10] NIHR Oxford Biomedical Research Centre, Second Floor, Unipart House Business Centre, Oxford, OX4 2PG, UK

[11] Human Immunology Unit, MRC Weatherall Institute of Molecular Medicine, University of Oxford, Oxford, OX3 9DS, UK

[12] Centre for Computational Biology, Institute of Cancer and Genomic Sciences, University of Birmingham, Birmingham, B15 2TT, UK

[13] Division of Informatics, Imaging and Data Sciences, Faculty of Biology Medicine and Health, The University of Manchester, Manchester, M13 9PT, UK

[14] Alan Turing Institute, London, NW1 2DB, UK

[15] These authors contributed equally

[16] Lead Contact

[*] Correspondence: ahmed.ahmed@wrh.ox.ac.uk (A.A.A), christopher.yau@manchester.ac.uk (C.Y)

Summary

The inter-differentiation between cell states promotes cancer cell survival under stress and fosters non-genetic heterogeneity (NGH). NGH is, therefore, a surrogate of tumor resilience but its quantification is confounded by genetic heterogeneity. Here we show that NGH in serous ovarian cancer (SOC) can be accurately measured when informed by the molecular signatures of the normal fallopian tube epithelial (FTE) cells, the cells of origin of SOC. Surveying the transcriptomes of ~6000 FTE cells, predominantly from non-ovarian cancer patients, identified six FTE subtypes. We used subtype signatures to deconvolute SOC expression data and found substantial intra-tumor NGH. Importantly, NGH-based stratification of ~1700 tumors robustly predicted survival. Our findings lay the foundation for accurate prognostic and therapeutic stratification of SOC.

Significance

Serous ovarian cancers represent the most common malignancies of ovarian carcinomas. Molecular stratification of high-grade serous ovarian cancer (HGSOC) has been difficult, presumably because of profound genetic heterogeneity limiting reproducible prognostic classifications. We now overcome this limitation by investigating the differentiation trajectory of non-cancer FTE cells using single-cell RNA sequencing and discovering four FTE secretory subtypes. Using the subtype molecular markers of non-cancer cells, we define a gene signature that robustly identifies a poor-prognosis EMT-high subtype of HGSOC. Conceptually, we show how examining non-cancer cells of origin could enable the accurate prediction of cancer behavior. Moreover, our work has important prognostic implications for ovarian cancer patients and enables future efforts for therapeutic optimization for EMT-high tumors.

Introduction

Intratumor heterogeneity is a key mechanism for survival and evolution of tumors (Brock et al., 2009; Marusyk et al., 2012). Genetic heterogeneity has been established as a mechanism of survival for most cancer types (Greaves and Maley, 2012; McGranahan and Swanton, 2017; Nowell, 1976). Additionally, cancer cells of the same genetic background may have different phenotypic cell states that enable essential tumor characteristics such as invasion, metastasis and resistance to chemotherapy (Brock et al., 2009; Pisco et al., 2013). The ability of cancer cells to change from one cell state to another (plasticity) is a key feature for cancer survival (Meacham and Morrison, 2013). While genetic heterogeneity is acquired, phenotypic heterogeneity is often inherited from the parent cell-of-origin of a tumor, due to epigenetic regulation or other mechanisms (Gupta et al., 2011; Visvader, 2011). Understanding cancer cell plasticity is dependent on the accurate identification and characterization of individual cell states. Recognizing that cancer cells have plasticity should be reflected on tumor stratification strategies that take into account the co-existence of multiple cancer cell states within any one tumor. However, the direct molecular characterization and identification of such states in a tumor is significantly confounded by genetic heterogeneity. An alternative approach for elucidating the phenotypic repertoire of a tumor type is to study the cell states of its cell-of-origin and use those characteristics to decompose an individual tumor into its constituents (Baron et al., 2016; Gupta et al., 2011; Newman et al., 2015).

High-grade serous ovarian carcinoma (HGSOC) is the most aggressive gynecological malignancy (Koshiyama et al., 2017), which is characterized by ubiquitous *TP53* mutations and frequent chromosomal alterations (Ahmed et al., 2010; Bell et al., 2011; Etemadmoghadam et al., 2009; Macintyre et al., 2018). One of the major challenges of HGSOC is the late presentation with almost 80% of patients diagnosed at Stage III or IV disease and a 5-year

survival rate of about 30% (Torre et al., 2018). The absence of robust methods to stratify HGSOC has been a challenge against therapeutic innovation. Previous studies demonstrated the transcriptomic heterogeneity of HGSOC (Bell et al., 2011; Tothill et al., 2008). However, analyses using bulk transcriptomes are confounded by a variety of factors, such as copy number variation (Macintyre et al., 2018) and infiltration by non-cancer cells. Importantly, such analyses do not take into consideration the possibility of multiple cell states co-existing in one tumor. Such confounding factors lead to unstable classifications with variable prognostic power across independent datasets (Chen et al., 2018). It is plausible to hypothesize that phenotypic states of the cell-of-origin of ovarian cancer may be echoed in daughter cancer cells. Linking basal and luminal cells from the mammary epithelium to corresponding breast cancer subtypes is a clear example of achieving a stable molecular classification based on understanding phenotypic diversity of the cell-of-origin. This approach has also been successful in other cancers (Fessler and Medema, 2016; Gilbertson, 2011; Ince et al., 2007; Wang et al., 2013).

Recent studies strongly support that SOC can originate from the fallopian tube epithelium (FTE) with evidence from mouse models and genetic evolutionary studies (Ducie et al., 2017; Kim et al., 2012; Labidi-Galy et al., 2017; Perets et al., 2013). Previous work reported that the FTE is composed of PAX8 positive secretory, TUBB4 positive ciliated and CD44 positive basal cells (Clyman, 1966). However, whether there are additional cellular subtypes and whether these subtypes are connected to subtypes of HGSOC have remained elusive. The advent of single-cell RNA sequencing (scRNA-seq) has enabled the identification of cellular subtypes (Grün et al., 2015). There are two major types of scRNA-seq techniques (Svensson et al., 2018); a) the droplet-based methods that have the advantage of high throughput (from 10 to 100 thousand cells) , such as InDrop (Klein et al., 2015), Drop-Seq (Macosko et al., 2015) and the commercially available 10x Genomics Chromium system and b) plate-based methods that

require fewer cells and have higher gene coverage, such as Smart-Seq2 (Picelli et al., 2014; Ziegenhain et al., 2017). Recent studies suggest that higher sequencing depth can compensate for a smaller sample size (Seirup et al., 2019; Svensson et al., 2019), and two studies have demonstrated that Smart-Seq2 can robustly identify cell states with relatively small sample sizes. Grün et al. sequenced only 238 cells from mouse intestinal organoids with the coverage of 3000 genes per cells, which enabled the identification of rare intestinal cell types (Grün et al., 2015; Patel et al., 2014); Patel et al. analyzed 430 cells from 5 human glioblastoma samples with the average coverage of 6000 genes per cell, which revealed the structure of transcriptional programs and cell phenotypes (Patel et al., 2014). Here, we characterized the cell subtypes of human fallopian tube epithelium by using this deep scRNA-seq technique; and investigated the association between the composition of bulk SOCs and prognosis.

Results

Culturing substantially alters single-cell transcriptomes

We first analyzed 3,877 single cells from the fallopian tubes of 5 ovarian cancer patients and 5 endometrial cancer patients using the Smart-Seq2 technique (Picelli et al., 2014) (Figures 1A, S1A and Table S1). Flow Cytometry was used to identify and sort single FTE cells ($EpCAM^+$, $CD45^-$), leukocytes ($EpCAM^-$, $CD45^+$) and stromal cells ($EpCAM^-$, $CD45^-$) prior to sequencing. To overcome the confounding batch effects and patient-specific variability in clinical samples, we used differential-expression-based clustering (Figure 1B and STAR Methods). Using this approach, we successfully differentiated between epithelial and non-epithelial cells (Figure 1C).

Cryopreservation and cell culture are common techniques to maintain live primary cells, especially for rare clinical samples. To test the effect of the cell maintenance approach, we compared the single-cell transcriptomes between fresh and cultured FTE cells. We observed

striking effects induced by culture conditions on the transcriptomes of single cells by comparing freshly dissociated cells with cultured ones (Figures S1B-H and Tables S2, S3). For example, overnight culture induced the expression of genes that are rarely expressed in FTE cells such as *CD44* ($\log_2$ fold-change [log-FC] = 3.8) (Paik et al., 2012) and reduced the expression of key markers of secretory cells, such as Estrogen Receptor alpha (*ESR1*) and Oviductal Glycoprotein 1 (*OVGP1*) (Figure S1F and Table S3) (Cerny et al., 2016; Wu et al., 2016). Cilium organization was also downregulated in the overnight-cultured ciliated cells. A recent study showed that the Wnt pathway is essential in regulating the homeostasis of FTE cells (Kessler et al., 2015). Our analysis showed that the expression level of *LGR5* decreased in secretory cells after overnight culture, in line with the previous finding that *LGR5* was not expressed in FTE organoids (Kessler et al., 2015) (Figure S1D-E). The expression of *RSPO1*, another key player in the Wnt signaling, was reduced after culture, suggesting that the Wnt signaling was affected by the culture condition. Moreover, pseudotime analysis (Campbell and Yau, 2018) across three conditions revealed that the transcriptomes of long-term (LT) cultured cells were more similar to the fresh cells compared to the overnight-cultured group (Figures 1D-E). For instance, the fatty acid metabolic process was transiently downregulated after overnight culture and then upregulated in the LT group, while the RNA processing pathway was upregulated temporarily (Figures S1B-C, G). This suggests that including the overnight-cultured cells in subsequent analysis may introduce significant biases that would preclude meaningful conclusions. Similarly, although the LT group resembled the fresh group of cells, they showed a unique split into two sub-groups and perturbed expression of Stathmin (*STMN1*) as well as cell cycle genes that probably represented an artefact of LT culture (Figures 1D, E and S1B, H). Therefore, overnight and LT culture likely introduced nontrivial alteration in gene expression. To avoid these substantial effects from preservation methods, we focused our downstream analysis on fresh cells only. Although fresh cells were affected by early response

genes (e.g. *FOS* and *JUN*), our analysis indicates that such affected cells can be detected by unsupervised clustering.

A cell census of human fallopian tubes in cancer patients

We partitioned the fresh FTE cells (2132) into two previously established subtypes: secretory (1986) and ciliated cells (146) (Figure 2A). Secretory cells were characterized by the expression of *PAX8* and *KRT7* (Figures S2A, B) as well as a large number of newly identified markers of secretory cells (Table S4). The ciliated population was represented by the strong expression of *FOXJ1* and members of the coiled-coil domain containing protein family, such as *CCDC17* and *CCDC78* (Figures S2C-D). This protein family is essential for cilia functioning (Klos Dehring et al., 2013). We also identified a list of previously unrecognized markers of fallopian tube ciliated cells (Table S4), such as the calcium binding protein Calcyphosin (*CAPS*), that were enriched in the cilium-related pathways (Figures S2B-C, E-F) (Wang et al., 2002).

We next identified secretory cell subtypes based on their transcriptomes. For this, only 1410 fresh secretory cells with strong expression of *KRT7* and *EPCAM* and no expression of *CCDC17* or *PTPRC* (also known as CD45) were included in the analysis. In addition, to avoid including potential contaminating cancer cells, we excluded the cells that had detectable copy number variants or apparent loss-of-heterozygosity (Figure S2G) (Fan et al., 2018). We applied the aforementioned differential-expression-based clustering method and identified nine clusters with distinct transcriptional profiles within the secretory cell population (Figures 2B-C, Table S5). Except for a patient-specific cluster (C8) that was enriched in inflammatory markers, all other clusters contained cells from multiple patients (Figures 2B and S2H-I). Cluster 8 was, therefore, not considered for further analysis. Three out of nine clusters (C1, C2

and C5) had no particular distinguishing features and clusters C1 and C2 had low library complexity (Figure S2J). This result suggests that these three clusters probably represented a quiescent population due to cell senescence or loss of hormonal influence (CROW et al., 1994; van Deursen, 2014). These clusters were, therefore, excluded from further analysis. Cluster C6 had evidence of cell stress as shown by the high expression levels of early response genes, such as *FOS* and *JUN* (Honkaniemi et al., 1992). This cluster was excluded from further analysis because such stress response is probably the result of sample preparation prior to sequencing.

Cluster C9, that we termed cell cycle cluster, comprised ~1.6% of fresh FTESCs and was enriched in three pathways, namely cell cycle (e.g. *MCM2-7*, *MKI67*, *TK1* and *STMN1*), DNA repair (e.g. *FANCD2*, *FANCI* and *MSH2*) and chromatin remodeling (e.g. *HMGB2* and *SMC1A*) (Figures 2C-E). *MKI67* (also known as Ki-67) is a well-known marker for proliferation in FTE and other cells (Kuhn et al., 2012). The two Fanconi Anemia proteins, FANCD2 and FANCI, can form a heterodimer that is essential for DNA repair and can interact with MCM2-7 (Nalepa and Clapp, 2018). The relatively low percentage of cycling cells is consistent with the ages and postmenopausal status of patients from whom the cells were obtained. Cluster C3, was termed the differentiated subtype, had significantly increased representation from genes involved in RNA synthesis and transport pathways (e.g. *PTBP1*, *ZNF259* and *PRPF38A*). It also shared several markers with cluster C9. This may represent a transient differentiating cell population following cell division.

Cluster C4, termed the KRT17 subtype, was characterized by the upregulated expression of major histocompatibility complex (MHC) Class II genes (e.g. *HLA-DQA1*, *HLA-DPA1* and *HLA-DPB1*), cytokeratins (*KRT17* and *KRT23*), aldehyde dehydrogenases (ALDHs, e.g. *ALDH1A1* and *ALDH3B2*) and *CDKN1A* (also called p21) (Figures 2C, F, Table S6). This

subpopulation of secretory FTE cells that were enriched in MHC Class II expression has not been characterized previously (Comer et al., 1998). Importantly, we validated this KRT17 positive cluster in human FTE and organoids derived from human FTE cells, suggesting that it represents a robust group of cells with potentially important biological functions (Figures 2G-I).

C7 showed high expression of a regulator of G protein signaling (*RGS16*) and genes enriched in the extracellular matrix (ECM) pathway (false discovery rate [FDR] = 1.80e-17), such as *TIMP3* and *SPARC* (Figures 2C, S2K-L and Table S6). We assumed that this cell type is generated by partial epithelial-mesenchymal transition (EMT) (Nieto et al., 2016), which can be induced by the chronic exposure to oxidative stress (Mahalingaiah et al., 2015) and contribute to cancer development (Hanahan and Weinberg, 2011). Hence, we termed C7 as the EMT subtype. To verify that this cell type is not a contamination from FT stromal cells, we checked the expression level of epithelial markers, doublet likelihood and the expression of stromal markers. This EMT population strongly expressed *KRT7* and *EPCAM* (Figure S2L) as expected following the aforementioned filtering. It also passed our filter for doublets; 40 (100%) out of 40 cells in the EMT cluster were detected as singlets (McGinnis et al., 2019). Moreover, two stromal markers (*COL1A2* and *COL3A1*) were specifically expressed in stromal cells but not in the EMT population (Figure S2M). These results demonstrate that this population is not contaminated by mesenchymal cells.

To exclude the potential paracrine effect of cancer cells on non-cancer FTE cells, we validated the existence of the four secretory subtypes in the FTE cells obtained from benign (non-cancer) donors. We first analyzed 1857 single-cell transcriptomes of fallopian tubes from five patients with benign conditions (Figures 3A, S3A-B and Table S1). Next we integrated the fresh

secretory cells from the benign patients with the annotated ones from cancer patients by computing batch-correcting anchors (Stuart et al., 2019). Clustering of the integrated data illustrated that the four secretory subtypes also existed in the FTE of non-cancer donors (Figures 3B-D). Further validation using immunofluorescence (IF) and immunohistochemistry (IHC) in FT samples from benign donors confirmed the above results (Figures S3C-E). Overall, these results demonstrate that the new secretory subtypes were not artefacts caused by the influence of nearby cancer cells or by systemic effects of cancer burden.

In addition to the four secretory cell types, we discovered a rare intermediate cell type that was characterized by the expression of the secretory cell marker KRT7 and high expression of the ciliated cell marker CAPS (Figures 4A-B and S4A-B), whilst other KRT7 positive secretory cells were CAPS negative. *PAX8* was expressed in a subset of this intermediate population, possibly due to its moderate expression level leading to a higher dropout rate. This population was validated in human FTE tissue sections (Figures 4A-B). Additionally, this subtype was enriched in overnight cultured cells and recapitulated in the organoid culture derived from human FTE tissues (Figure 4C). This intermediate population most probably represents an intermediate state between secretory and ciliated cells, which accords with the previously assumed transition from secretory to ciliated cells (Ghosh et al., 2017; Hellner et al., 2016).

Because we observed that chemokines and MHC genes were frequently expressed in FTE cells (Figure 2B), we examined fallopian tube sections for the expression of lymphocyte markers and identified a basal $CD45^+$ $EpCAM^+$ cell population. This population was also positive for CD3, CD44, CD69 and CD103 (Figures 4D-H), suggesting that these basal cells are tissue-resident memory T lymphocytes (TRMs) (Topham and Reilly, 2018) and that the FTE is not immunologically inert. This is in line with previous studies (Ardighieri et al., 2014; Peters,

1986). Nevertheless, we demonstrate that this basal cell population was also EpCAM positive, which is surprising because TRMs have not been reported to be positive for epithelial markers in human.

Revealing the cell state composition of HGSOCs using deconvolution

Given the link between types of cell-of-origin and tumor types that has been reported in other cancers such as breast cancer (Bertucci et al., 2012; Dai et al., 2015) and the known shared key markers between HGSOC and FTE cells (e.g. *PAX8*, *WT1* and *ESR1*) (Ince et al., 2015; Perets et al., 2013), we hypothesized that HGSOC cell states are linked to FTE cell subtypes. Based on our profiling of single-cell transcriptomes, we computed a reference matrix with cell-type derived transcriptomic signatures from the five major FTE cellular subtypes (cell cycle, EMT, differentiated, KRT17 cluster and ciliated) as previously described (Baron et al., 2016) (Figure 5A and Table S7). The resulting reference matrix was then used in the deconvolution analysis (Newman et al., 2015) of the bulk HGSOC RNA-seq data from The Cancer Genome Atlas (TCGA) (Bell et al., 2011) and the microarray data from the Australian Ovarian Cancer Study (AOCS) (Tothill et al., 2008) to compute the factions of five cell states within each tumor. The decomposition of bulk tumor samples revealed intra-tumor transcriptomic heterogeneity according to the proportions of cell subtypes in both datasets (Figures 5B-E). Remarkably, the ciliated tumor subtype was highly enriched in the low-grade tumors (Grade 1) compared to the high-grade ones (Grades 2-3) in the AOCS dataset and an additional dataset that also comprised both high- and low-grade tumors (Yoshihara et al., 2010) ($p = 1.3e-10$, one-sided Wilcox test, Figures 5F and S5). This strongly suggests that grades of SOC are associated with their ability to differentiate into cells that molecularly resemble FTE ciliated cells. In contrast, the TCGA dataset, which only included HGSOCs, had no tumors that were enriched in the ciliated subtype (Figure 5B). Therefore, the enrichment in these ciliated markers is most probably a

distinguishing molecular feature of low-grade tumors.

Most notably, we identified a class of EMT-enriched tumors in multiple datasets. These tumors were enriched in the genes previously linked to the "mesenchymal" HGSOC subtype. We found that the marker genes of these tumors were enriched in the extracellular matrix, focal adhesion and PI3K-Akt signaling pathways (FDR < 0.0002, by DAVID, Table S8), that are critical for tumor cell survival (Fresno Vara et al., 2004; McLean et al., 2005). Furthermore, three key EMT transcription factors, *TWIST1*, *TWIST2* and *SNAI2* (Ansieau et al., 2008; Kang and Massagué, 2004; Yang et al., 2004), were upregulated in the EMT-high tumors (Figure 5G), while the miRNA-200 family (miR-200a, miR-200b, miR-200c, miR-141 and miR-429) that represses EMT (Gregory et al., 2008; Nieto et al., 2016) was downregulated in EMT-high tumors (FDR < 0.01, log-FC < -0.5, Figure 5H), suggesting that EMT may be the underlying mechanism of enrichment of mesenchymal cancer cells in this tumor subtype. We also found that miRNA-483 and miRNA-214 were significantly upregulated in EMT-high tumors, while miRNA-513c, miRNA-509 and miRNA-514 were downregulated (Figure 5H). Although previous studies suggested that miRNA-483 and miRNA-214 play an important role in cancer progression (Chandrasekaran et al., 2016; Liu et al., 2013), their regulatory role in the EMT process has not been evaluated.

EMT-high subtype is robustly correlated with poor prognosis

We next tested whether any of the five tumor subtype scores from the deconvolution analysis was associated with survival. We found that the EMT score was significantly associated with poor overall survival and that this association was independent from the effect of age, stage or residual disease ($p < 0.05$, by Cox proportional hazard model, Table 1). The robustness of this association was confirmed by permutation testing (n = 500) leaving out 10% of the samples

each time (empirical p values = 0.012 [TCGA] and 0 [AOCS], by permutation test). The mesenchymal subtype was previously reported to be associated with poor prognosis (Konecny et al., 2014; Tan et al., 2013), but the reproducibility of this observation was inconsistent probably because of the difficulty in defining this group of tumors. We first compared the prognosis of EMT-high tumors with the previously defined "mesenchymal" HGSOC subtype in the TCGA data. The analysis showed that the EMT score had higher sensitivity of identifying poor-prognostic patients (Figure S6A). Importantly, among the 238 cancers that were labeled as non-mesenchymal in TCGA we identified 87 tumors that were EMT-high. These tumors carried worse prognosis when compared with the non-mesenchymal and EMT-low group of cancer. Furthermore, by using EMT scores from deconvolution, we reached a robust classification with consistently significant correlation with poor survival ($p < 0.05$) in eight independent datasets, including TCGA dataset, AOCS dataset and six additional microarray datasets ($n > 100$ patients in each set) from the CuratedOvarianData database (Ganzfried et al., 2013) (Table 1 and Table S9). When we combined and dichotomized all the samples ($n = 1,626$), the EMT-high tumors had significantly worse prognosis ($p = 5.92e-10$, hazard ratio = 1.5, 95% confidence interval [CI] = 1.3 – 1.7, by log-rank test, Figure 6A). This demonstrates that deconvolution analysis using the identified panel of genes is strongly predictive of prognosis in SOC.

To test whether the EMT-high tumor subtype was merely a reflection of stromal cell impurities in tumor samples, we performed RNA sequencing on 36 laser capture microdissected (LCM) tumor samples collected from 15 patients with HGSOC (termed the Oxford Ovarian Cancer-Predict Chemotherapy Response [OXO-PCR] cohort) and classified tumors based on the deconvolution analysis (Figure 6B). We next compared the expression of genes in the EMT signature between laser capture microdissected tumor and stroma samples. As expected, the

expression levels of *PAX8* and *EPCAM* were significantly higher in both EMT-high and EMT-low tumor samples compared to stroma in which these markers showed almost no expression (Figure S6B). In contrast, the EMT markers (*SPARC*, *TIMP3*, *DCN* and *SFRP4*) were highly expressed in EMT-high tumor confirming that EMT-high tumors truly expressed these genes (Figure 6C), further confirming EMT-high as a genuine tumor subtype. *SPARC*, one of the 12 genes that constitute the EMT signature, was previously described in the mesenchymal subtype of HGSOC (Tothill et al., 2008), while certain other markers were reported to be related to EMT in ovarian cancer or other cancers, such as *SFRP4* (Ford et al., 2013), *TIMP3* (Anastassiou et al., 2011), *MYH11* (Li and Yang, 2016) and *EFEMP1* (Yin et al., 2016). Nevertheless, the link between this tumor subtype and a particular FTE cellular subtype was previously unrevealed. To further confirm that the EMT-high marker SPARC is strongly expressed in cancer cells, we performed immunofluorescent staining on pre-chemotherapy tumor frozen sections, where we indicated cancer cells by co-staining with an antibody that recognized pan-cytokeratin. Our results revealed the co-existence of at least two populations of cancer cells, a pan-cytokeratin high, SPARC negative population and a pan-cytokeratin low and SPARC positive population within the same tumor (Figures 6D, S6C and Video S1). In addition, pan-cytokeratin negative and SPARC high cancer cells could also be identified by their abnormal nuclei (Figures 6E and S6D), which were distinct from the SPARC high fibroblasts cells (Tan et al., 1999). We also confirmed the expression of SPARC in p53 positive tumor cells by performing IHC on p53-expressing HGSOC samples (Figures S6E-F).

Similarly, this SPARC positive, pan-cytokeratin negative and mesenchymal-like subpopulation was observed in the KURAMOCHI cell line, which is known to faithfully represent HGSOC (Domcke et al., 2013). KURAMOCHI cells exhibited two phenotypes, a mesenchymal-like phenotype that was SPARC positive and pan-cytokeratin negative and an epithelial phenotype

that was SPARC negative and pan-cytokeratin positive (Figures 6F and S6G-H), suggesting that this cell line could be a potential *in vitro* model to study the mesenchymal subtype of HGSOC. Importantly, SPARC positive cells expressed p53 (Figure S6I) providing further confirmation of the existence of EMT-high cancer cells. Moreover, TP53 sequencing of this cell line showed a single peak for the previously described mutation (c.841G>T) in this cell line (Anglesio et al., 2013), validating that the phenotypic heterogeneity was not caused by contamination with another cell line.

Discussion

In this study, we performed deep single-cell RNA-seq on thousands of nonmalignant epithelial cells from the FTE and uncovered a strong link between diverse secretory cell populations and HGSOC subtypes. This elucidates the repertoire of phenotypic heterogeneity in cancer cells that are inherited from the cell-of-origin. We propose a model whereby individual HGSOCs are composed of a mixture of cancer cell states that we revealed by single-cell sequencing of the putative cell-of-origin (Figure 7). Unraveling the trajectory of differentiation from one cancer cell state to another will be needed in future studies to understand the mechanistic basis of HGSOC cell plasticity.

Within the FTE, our analyses recognized a KRT17 positive population with high expression of ALDHs and MHCII. ALDH was reported as the marker of mammary stem cells (Biton et al., 2018; Ginestier et al., 2007). Moreover, a subpopulation of intestinal stem cells was recently reported to express MHCII. The latter was found to regulate the stem cell fate through the interaction between T helper cells and stem cells (Biton et al., 2018; Ginestier et al., 2007). Such evidence implies that the KRT17 cluster that we identified could include a progenitor population. This opens a door for studying self-maintenance and differentiation of epithelial

cells in fallopian tubes.

Phenotypic diversity exists in HGSOC at the transcriptomic level (Bell et al., 2011; Tothill et al., 2008). Based on the single-cell profiling of FTE cells, our deconvolution analysis revealed the association between the FTE cellular subtypes with ovarian cancer cell states within individual tumors. The correspondence between tumors and normal tissues can be explained by at least two hypotheses that are not necessarily mutually exclusive. The first one is that each tumor subtype originates from an individual cell type of origin (Ince et al., 2007; Visvader, 2011). The second hypothesis is that multiple tumor subtypes come from one single cellular subtype, sometimes referred to as the cancer stem cell, while the plasticity of cancer cells mimics that of the normal cell-of-origin (Gupta et al., 2011; Visvader, 2011). Both concepts are compatible with our findings. Lineage tracing will be needed to investigate the underlying mechanism of the correspondence between tumors and the tissue-of-origin. Although the FTE plays as a strong candidate for the cell-of-origin of HGSOC, there is a possibility that the ovarian surface epithelium gives rise to a proportion of HGSOC cases as supported by the mouse model (Zhang et al., 2019b). The association between ovarian surface epithelium and HGSOC has not been addressed by our work.

Despite the fact that the mesenchymal-like tumor subtype was previously reported as a distinct subtype in HGSOC (Tothill et al., 2008), it has been controversial whether the expression of EMT markers originated from tumor cells, infiltrating stromal cells or both (Schwede et al., 2018; Zhang et al., 2019a). Our results demonstrate that the expression of mesenchymal-related genes, such as *SPARC*, occurs in tumor cells. This further supports the existence of the EMT process in human tumors, which may enhance their invasion ability and drug resistance (Schmidt et al., 2015; Singh and Settleman, 2010). This notion is consistent with our finding

that the EMT-high HGSOC subtype is related to poor survival. However, we cannot exclude the possibility that the expression of EMT genes in bulk tumor analyses may arise from stromal infiltration or cancer-associated fibroblasts (CAFs). Since CAFs can potentially promote cancer progression (G. M. Chen et al., 2018; Kalluri, 2016; Schwede et al., 2018; Eckert et al., 2019), it will also be important to scrutinize the role of CAFs in HGSOC and the interaction between CAFs and ovarian cancer cells.

Compared to the previously developed prognostic signatures of HGSOC that were difficult to be reproduced in multiple datasets (Bell et al., 2011; Bonome et al., 2008; Chen et al., 2018; Jiang et al., 2006; Karlan et al., 2014; Konecny et al., 2014), our classifier (we term, the Oxford classifier of serous ovarian cancer) is strongly reproducible across eight independent datasets and is based on the expression of only fifty-two marker genes. Robust identification of tumor subtypes is a prerequisite for identifying treatment strategies that limit the ability of cancer cell to acquire a mesenchymal state (Davis et al., 2014; Ishay-Ronen et al., 2019). Given these factors, our approach possesses potential translational significance to improve the survival of HGSOC patients.

In conclusion, our single-cell profiling illuminates the cellular landscape of human fallopian tube epithelium, the presumed tissue-of-origin of HGSOC. Our work not only expands the understanding of FTE, but also provides a benchmark dataset on FTE to study HGSOC. The combined analysis of single-cell data and tumor expression data revealed the connection between FTE cellular subtypes and HGSOC tumor subtypes and identified the EMT-high subtype with important prognostic implications.

Acknowledgements

We thank the WIMM Flow Cytometry Facility, Single Cell Facility, CBRG and Wolfson Imaging Centre for their help in this study. We thank the Oxford Radcliffe Biobank and the Oxford Centre for Histopathology Research for their help with obtaining tissue samples. This work was supported by Ovarian Cancer Action and Oxford Biomedical Research Centre (BRC), National Institute of Health Research. C.Y. was supported by a UK Medical Research Council Research Grants (MR/L001411/1, MR/P02646X/1), a Wellcome Trust Core Award Grant Number 090532/Z/09/Z and by The Alan Turing Institute under the EPSRC grant EP/N510129/1. Z.Y was supported by the NIHR Oxford BRC. D.M.P. was funded by the NIHR Oxford BRC (Molecular Diagnostics Theme/Multimodal Pathology Subtheme). Y.F. was supported by the CRUK Oxford Centre.

Author Contributions

Conceptualization, Project Administration and Supervision, A.A.A. and C.Y.; Funding Acquisition, A.A.A., C.Y. and Y.F.; Investigation, A.A.A., C.Y., Z.H., M.A., A.A., N.W., M.M., L.S.G., S.E., M.K., G.M., T.S., Z.Z., K.M., Y.Z., K.C., V.C. and T.S.S.; Data Curation, A.A.A., C.Y., Z.H. and M.A.; Methodology and Formal Analysis and Visualization, A.A.A., C.Y. and Z.H.; Writing – Original Draft, A.A.A., C.Y., Z.H., M.A. and A.A.; Writing – Review and Editing, A.A.A., C.Y. and Z.H.; Resources (Clinical samples), M.M., S.D., S.D., V.R., R.G.C., H.S., D.M.P. and S.J.

Declaration of Interests

A.A.A., C.Y., and Z.H. have filed a patent application for the use of the 52-gene panel for predicting the prognosis of ovarian cancer.

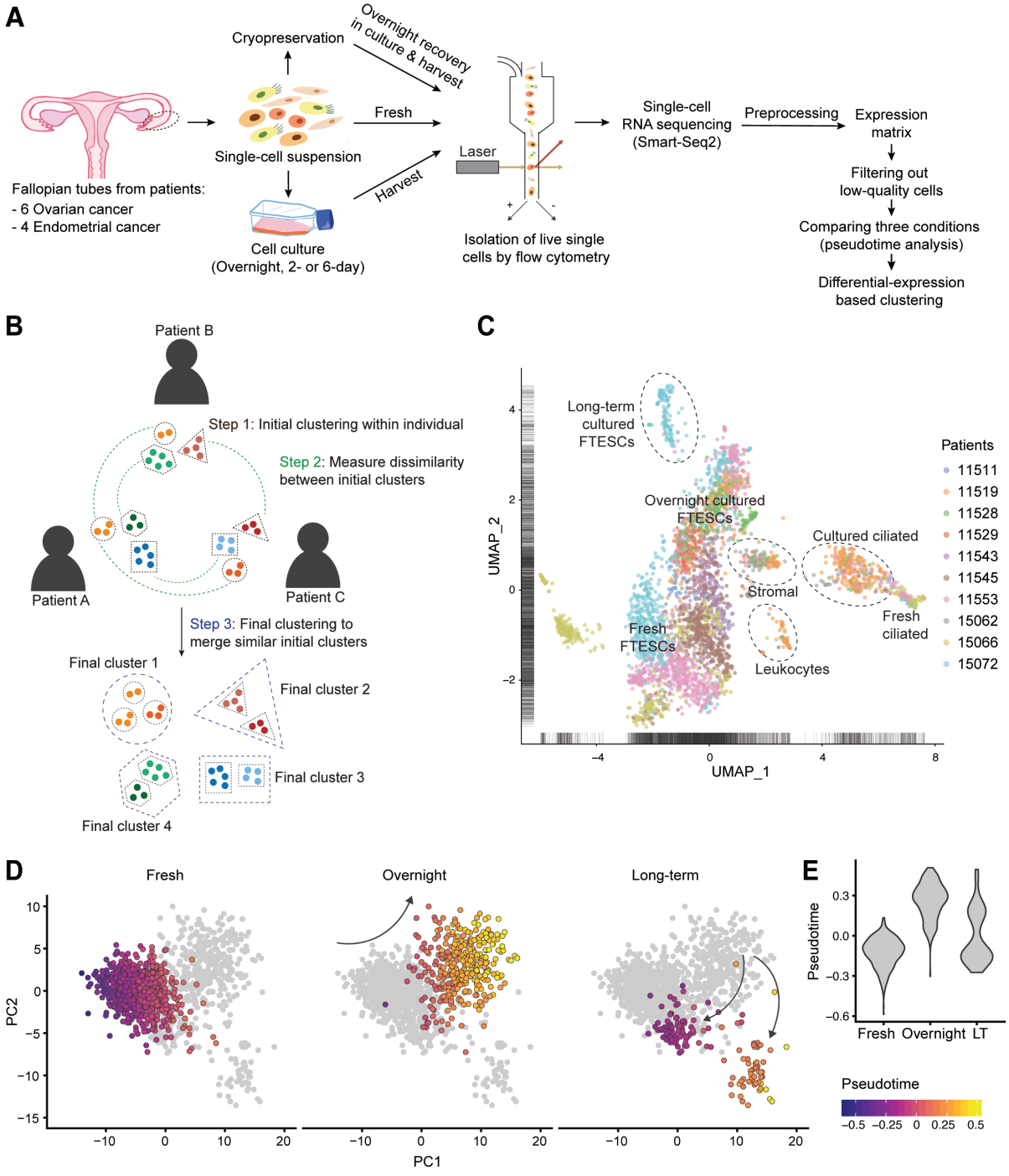

Figure 1. A cell census of human fallopian tubes.

(A) Diagram shows the single-cell RNA sequencing and analysis workflow. We collected and processed normal fallopian tube tissues from 10 cancer patients. All cells (directly sorted or maintained then sorted) were processed using with the Smart-Seq2 protocol. After the initial filtering, there were 3877 good-quality cells left for downstream analysis. We compared the cells from three conditions to select the optimal condition for single-cell RNA-seq. Cells from cultured or cryopreserved conditions, as well as cells carrying copy number variations and non-

epithelial cells, were filtered out, which left 2132 fresh FTE cells. Next, we used differential-expression-based clustering to identify secretory subtypes.

(B) Diagram shows the clustering approach. Three steps are used to overcome the confounding batch effects and inter-patient variability.

(C) UMAP shows the dimensionality reduction of ~3,800 single-cell transcriptomes from fallopian tube cells. The cells are colored by their patient sources and annotated with cluster names.

(D) Principal component (PC) analysis plot shows the cells under different conditions (fresh, overnight cultured and LT cultured) colored by the imputed pseudotime values.

(E) Violin plot shows the distribution of pseudotime under different conditions. The y-axis corresponds to the predicted pseudotime and the x-axis the conditions. Pseudotime analysis is defined as the quantification of pseudo-temporal ordering by projecting high-dimensional data to one dimension.

See also Figure S1; Tables S1-S3.

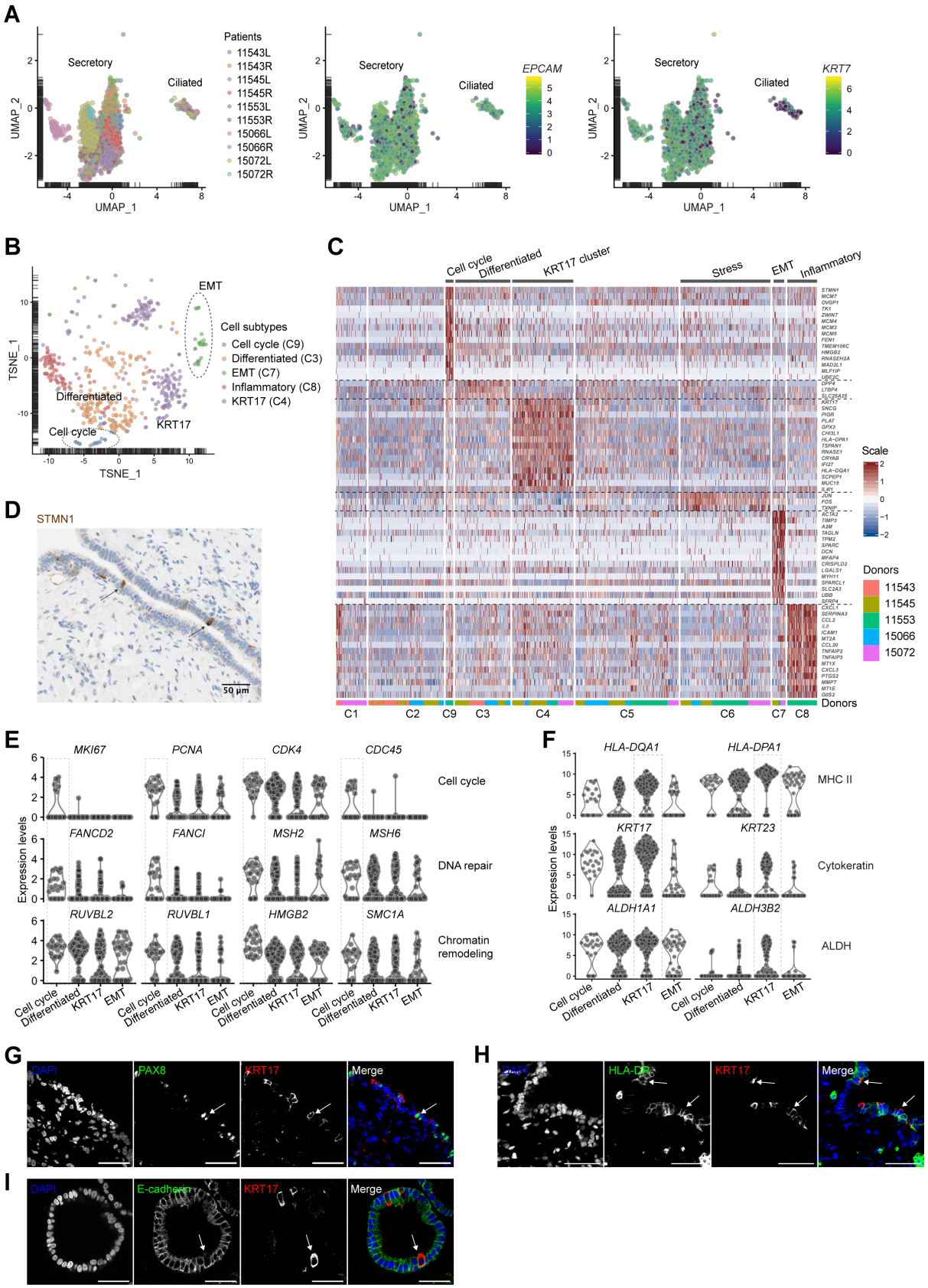

Figure 2. Single-cell RNA sequencing of FTE cells identifies four secretory subtypes.

(A) UMAP plots of fresh FTE cells show the difference between secretory and ciliated cells. Each dot denotes one cell. The cells are colored by donors and the side of tubes (left panel),

the expression levels of an epithelial marker, *EPCAM* (middle panel), and a secretory marker, *KRT7* (right).

(B) t-Distributed Stochastic Neighbor Embedding (t-SNE) plot shows the clusters within fresh secretory cells. Each point represents one cell that is colored by its cluster/subtype as shown in the legend. The quiescent population and the stress population are not shown in this plot.

(C) Heatmap shows the clustering result of fresh secretory cells and the expression levels of their top marker genes. Each column represents a single cell and each row represents a top marker gene. Colors indicate the expression levels as shown in the scale bar. The color bar at the bottom denotes the donors.

(D) IHC staining confirms the existence of the cell cycle cluster (arrows) by its marker STMN1 (Stathmin) in a human fallopian tube section.

(E) Violin plots show the expression of nine representative marker genes of the Cell Cycle Cluster (C9) that are respectively related to the cell cycle, DNA repair or chromatin remodeling pathways. Each dot is one cell.

(F) Violin plots show the expression of six representative marker genes of the KRT17 cluster (C4) that respectively belong to MHCII, cytokeratins or ALDHs.

(G-H) IF staining using the antibodies against KRT17 with PAX8 (G) or HLA-DR (H) in the human fallopian tube sections. Scale bars, 50 μm.

(I) IF double staining of KRT17 and an epithelial marker E-cadherin in the organoid derived from human FTE. Scale bars, 50 μm.

See also Figure S2; Tables S4, S5 and S6.

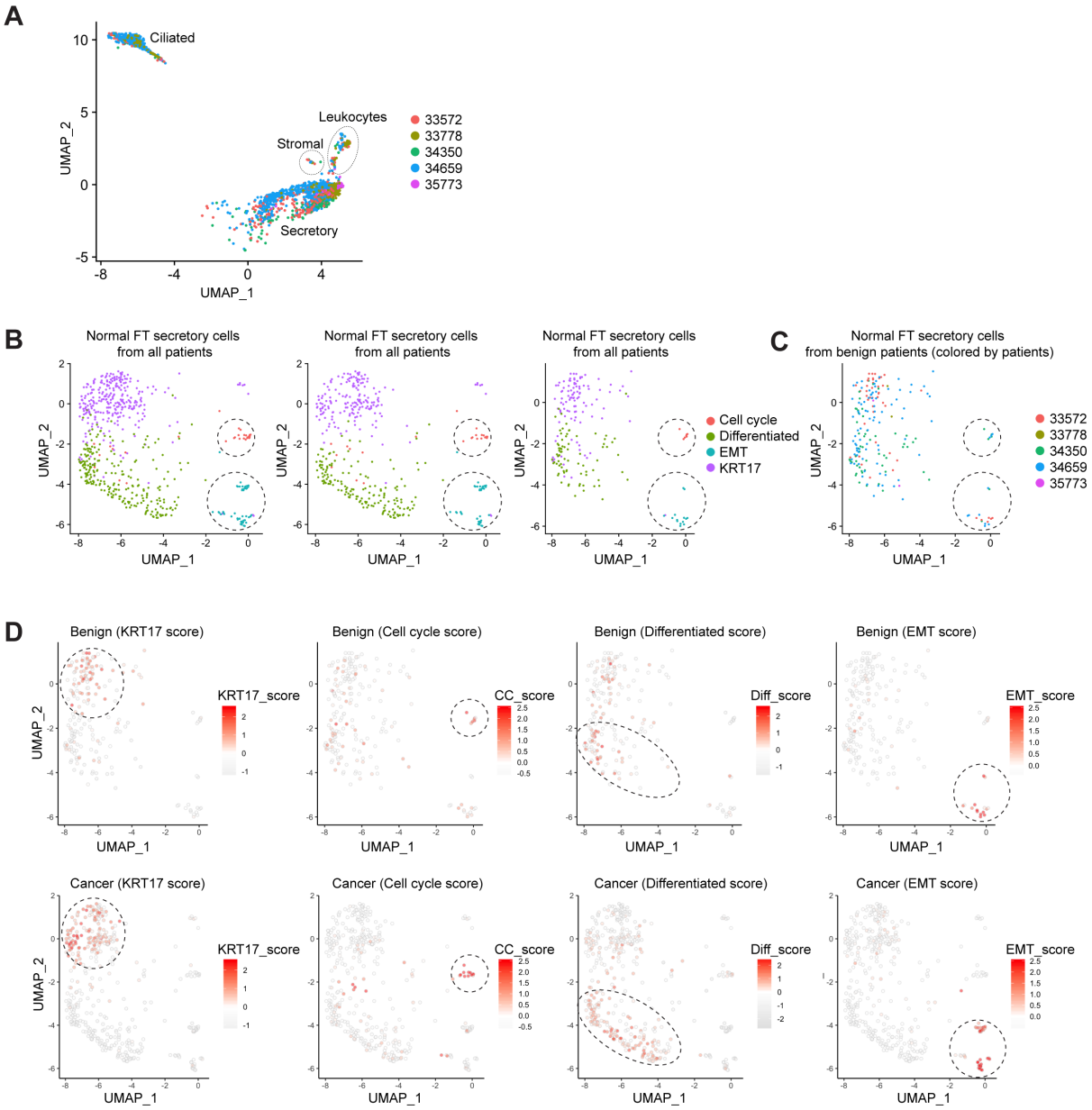

Figure 3. Validation of the secretory subtypes in the FTE of benign donors by using scRNA-seq.

(A) UMAP shows the populations in the FT samples from 5 benign patients. Each dot is a cell colored by its donor.

(B) UMAP plots show the populations in the FT samples from cancer patients (n = 5) and benign patients (n = 5). The left, middle and right subpanels contain the cells from all 10 patients, 5 cancer patients and 5 benign patients respectively.

(C) UMAP plot shows the populations in the FT samples from 5 benign patients. Each dot represents a secretory cell from a benign patient. The dots are colored by their donors as shown in the legend.

(D) Scatter plots show the transcriptomic characteristics of each subtype in benign and cancer patients. Cells (dots) are colored by the score of each transcriptomic signature (subtitle). The score of a transcriptomic signature was computed by the scaled and centered sum of expression levels of the marker genes in each transcriptomic signature. The scores correspond to the expression of marker genes of each cluster. The transcriptomic signatures are listed in Table S7.

See also Figure S3.

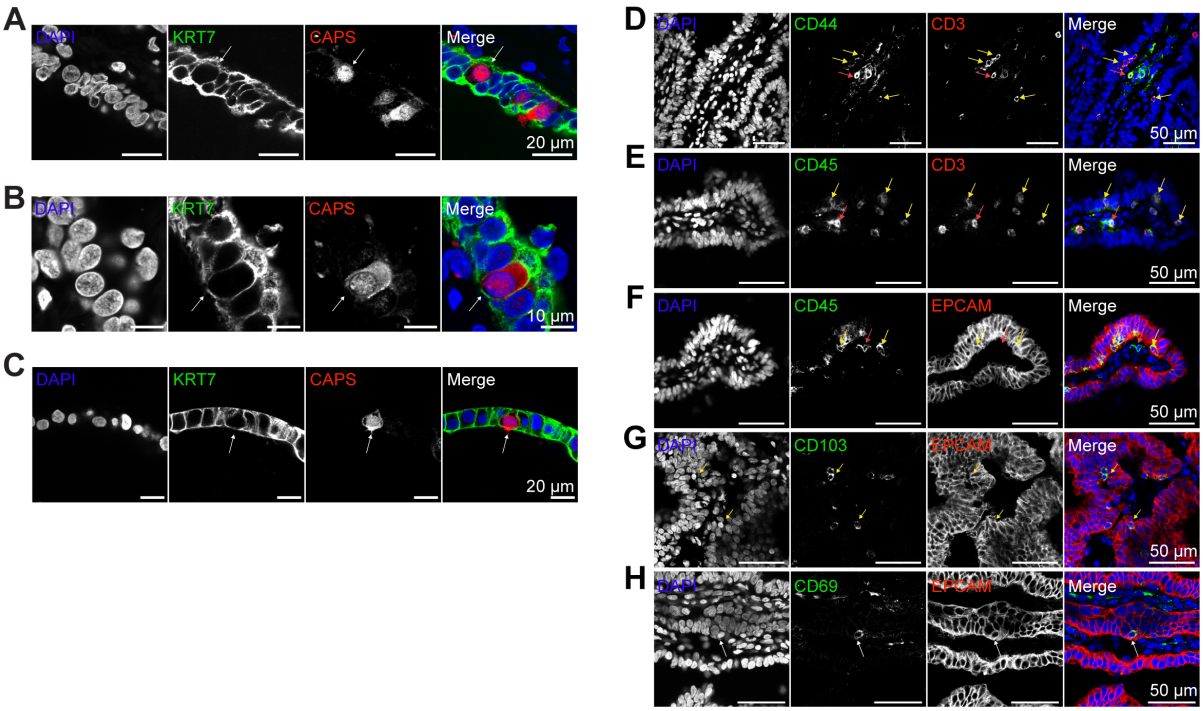

Figure 4. Non-traditional cell subtypes in the fallopian tube epithelial layer.

(A-B) IF staining for KRT7 and CAPS in human FTE samples (A and B). Arrows indicate the double positive intermediate cell population.

(C) IF staining for KRT7 and CAPS in the cultured human fallopian tube organoid. Arrow indicates the $KRT7^{+}$ $CAPS^{+}$ intermediate cell population.

(D-F) IF staining of CD44 and CD3 (D), CD45 and CD3 (E) as well as CD45 and EpCAM (F) in human FTE. Yellow arrows indicate the intra-epithelial $CD44^{+}$ $CD3^{+}$ cells that are also $CD45^{+}$ and $EpCAM^{+}$. Red arrows indicate the extra-epithelial $CD44^{+}$ $CD3^{+}$ $CD45^{+}$ $EpCAM^{-}$ cells in the stromal region.

(G-H) IF staining for EpCAM and two markers of tissue-resident memory T lymphocytes, CD103 (G) and CD69 (H), in the human FTE.

See also Figure S4.

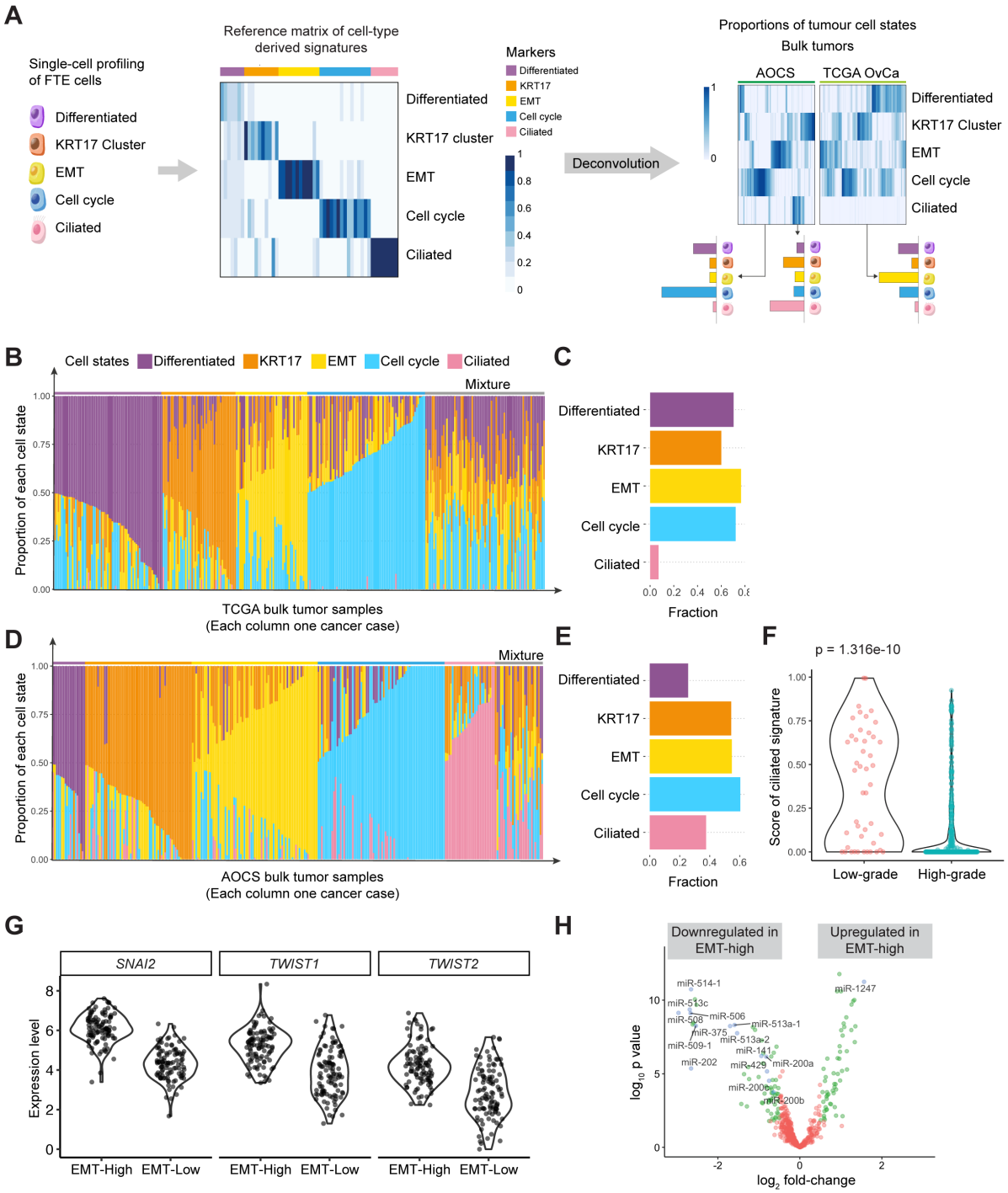

Figure 5. The repertoire of phenotypic heterogeneity of serous ovarian cancer revealed by deconvolution analysis.

(A) A reference matrix was calculated from our scRNA-seq data of FTE cells, where columns correspond to 5 cell subtypes in FTE as indicated. The reference matrix heatmap depicts the magnitude of the expression levels of the 52 marker genes (rows) across 5 cell subtypes, including 7 differentiated markers, 10 KRT17 cluster markers, 12 EMT markers, 15 cell cycle markers and 8 ciliated markers. The heatmaps in the right panel depict the proportions of cell states (rows) across bulk tumor samples (columns) in AOCS and TCGA datasets. Beneath these

heatmaps, three cartoon barplots that correspond to three samples show a schematic composition of these samples.

(B) Stacked barplot shows the deconvolution result of 308 tumors from the TCGA ovarian carcinoma study. Colors of the bars denote 5 cell states as shown in the legend. The y-axis represents the proportion of each state in a given bulk tumor sample. In the x-axis, each column represents one tumor case. The annotation bar above denotes the subtypes of bulk tumors that are defined by the dominant cell state within each tumor, where grey represents the mixture of multiple cell states.

(C) Barplot shows the prevalence of 5 cell states in the TCGA dataset. The x-axis represents the proportion of tumor samples in TCGA that harbor the given cell state (y-axis).

(D) Stacked barplot shows the deconvolution result of 285 tumors from the AOCS dataset as in B.

(E) Barplot shows the prevalence of 5 cell states in the AOCS dataset.

(F) Violin plot shows the ciliated scores in low-grade SOC compared to HGSOC. We combined samples from both AOCS (20 low-grade, 260 high-grade) (Tothill et al., 2008) and GSE17260 (26 low-grade, 84 high-grade) (Yoshihara et al., 2010). Each dot is one sample, colored by the grade. p = 1.3e-10, by one-sided Wilcoxon rank-sum test.

(G) Violin plots show expression of *TWIST1*, *TWIST2* and *SNAI2* in the EMT-high tumors compared to the EMT-low ones in the TCGA dataset (log-FC > 1.8, FDR < 2e-14, by limma voom).

(H) Volcano plot shows the miRNAs that are differentially expressed between EMT-high and EMT-low tumors in the TCGA dataset. The green and blue dots correspond to the miRNAs that are significantly differentially expressed (log-FC > 0.5, FDR < 0.05).

See also Figure S5 and Table S7.

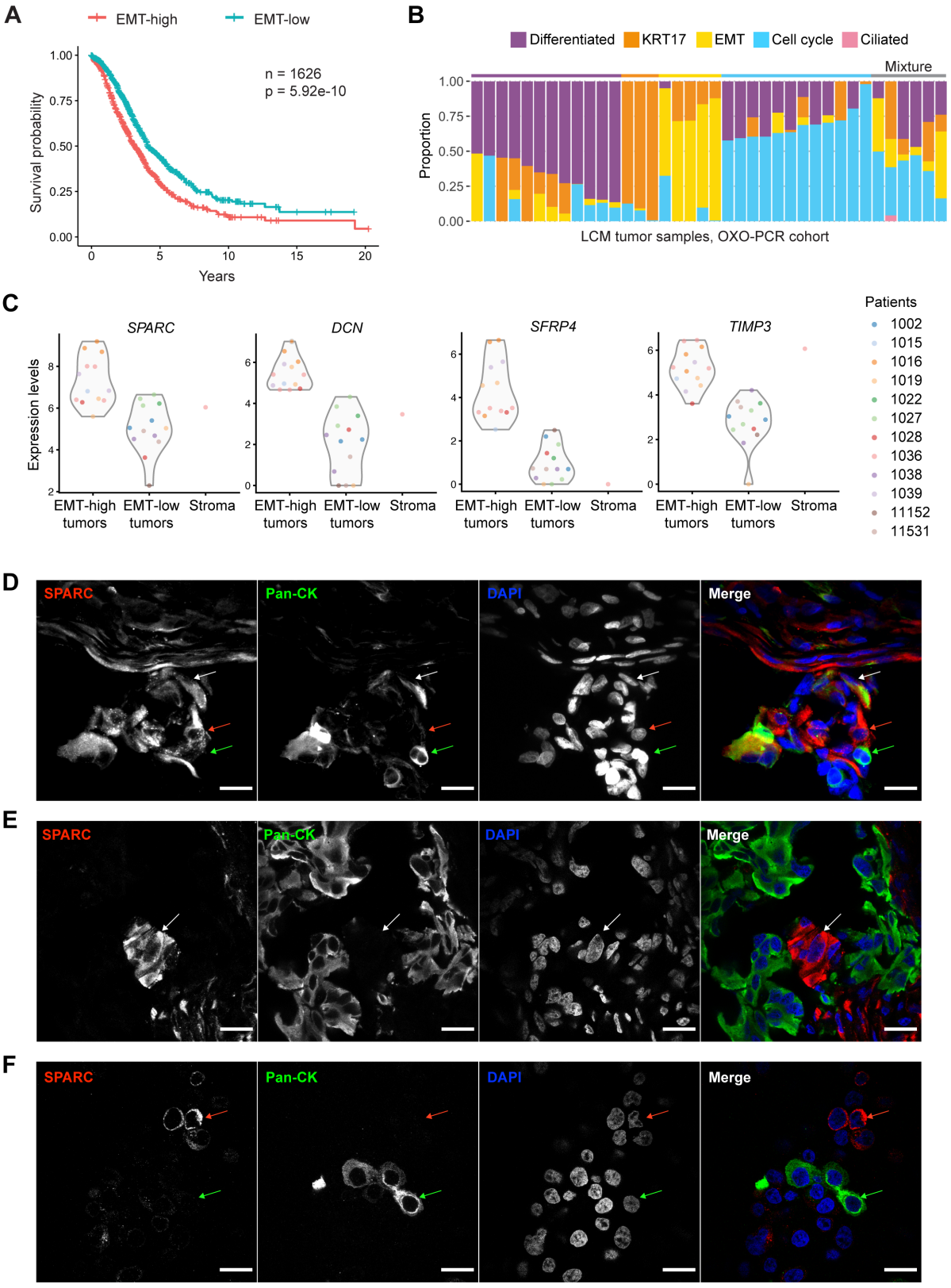

Figure 6. EMT-high tumors comprise mesenchymal-like cancer cells.

(A) Kaplan-Meier curves show the effect of EMT scores on survival. The cases of SOC (n = 1626) are combined from nine datasets (Table 1). Patients are dichotomized into EMT-high and EMT-low by the median of EMT scores in each dataset. Each short vertical line indicates a

censoring event. p = 5.92e-10, hazard ratio = 1.5 (95% CI 1.3 - 1.7), by log-rank test.

(B) Stacked barplot visualizes the deconvolution result of 36 LCM tumor samples collected from 15 patients with HGSOC in the OXO-PCR cohort. The y axis denotes the proportion (0-1) of the 5 cell states (colors) across LCM tumor samples (rows). The annotation bar above the barplot corresponds to the tumor subtypes that are defined by the dominant cell state within each tumor, where grey represents the mixture of multiple cell states.

(C) Violin plots show the expression levels of four EMT markers in the EMT-high LCM tumor samples compared to the EMT-low ones with one LCM stromal sample as control ($p < 0.001$, one-sided Wilcox test). Each dot is a sample colored by patients.

(D) IF staining in the pre-chemotherapy HGSOC tumor frozen section, using an EMT marker, SPARC, and an epithelial marker, pan-cytokeratin (Pan-CK). White arrow indicates cells that are double positive for SPARC and Pan-CK; red arrow indicates cells that are $SPARC^+$ only; yellow arrow indicates cells that are Pan-CK^+ only. Scale bars, 20 μm.

(E) IF staining for SPARC and Pan-CK in the pre-chemotherapy HGSOC tumor frozen section. Arrow shows a tumor cell that is $SPARC^+$ and Pan-CK^-. Scale bars, 20 μm.

(F) IF staining for SPARC and Pan-CK in the KURAMOCHI cell line. Red arrow indicates cells that are $SPARC^+$ and Pan-CK^-; green arrow indicates cells that are $SPARC^-$ Pan-CK^+. Scale bars, 20 μm.

See also Figure S6; Table S8; Video S1.

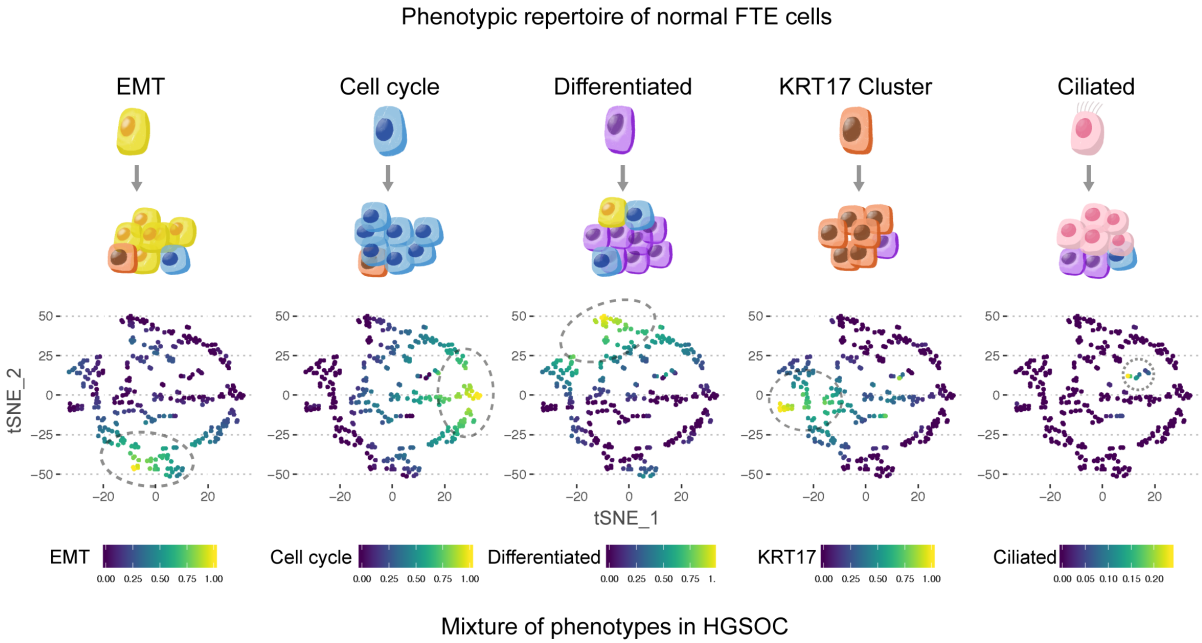

Figure 7. HGSOCs are composed of a mixture of cancer cell states inherited from its cell-of-origin in the FTE. The diagram proposes a model that HGSOCs are assembled from multiple cancer cell states that echo the cellular phenotypes of its tissue-of-origin. The upper panel exhibits 5 cellular subtypes of FTE. In the lower panel, 5 t-SNE plots demonstrate the cell state hubs within the deconvolution result of TCGA data. Each dot is a HGSOC bulk sample. The color scale denotes the proportion of cancer cell states. Grey dashed circles highlight the hubs representing the tumor subtypes of SOC.

Table 1. EMT-high serous tumors are robustly correlated with poor prognosis.

Dataset	Samples	Hazard ratio	p	95% CI	Citation
E.MTAB.386	128	3.11	0.018	1.21 – 7.95	(Bentink et al., 2012)
GSE49997	170	2.83	0.022	1.16 - 6.88	(Pils et al., 2012)
GSE13876	144	2.96	0.011	1.28 – 6.83	(Crijns et al., 2009)
GSE26712	185	2.03	0.031	1.07 – 3.89	(Bonome et al., 2008)
GSE26193	79	2.58	0.041	1.04 – 6.42	(Mateescu et al., 2011)
GSE51088	113	2.09	0.022	1.11 - 3.92	(Karlan et al., 2014)
GSE32062.GPL6480	260	1.89	0.055	0.99 - 3.60	(Yoshihara et al., 2012)
AOCS	253	2.11	0.008	1.21 - 3.67	(Tothill et al., 2008)
TCGA	305	2.12	0.011	1.18 – 3.81	(Bell et al., 2011)

See also Table S9.

STAR Methods

LEAD CONTACT AND MATERIALS AVAILABILITY

Further information and requests for resources should be directed to and will be fulfilled by the Lead Contact, Ahmed Ahmed (ahmed.ahmed@wrh.ox.ac.uk). This study did not generate new unique reagents.

EXPERIMENTAL MODEL AND SUBJECT DETAILS

Cell line

KUARMOCHI cell line (cell number ID: JCRB0098) was obtained from Japanese Collection of Research Bioresources (JCRB) Cell Bank. KURAMOCHI cells were cultured in RPMI 1640 media (Gibco) with Fetal Bovine Serum (FBS, 10%; Gibco) and Penicillin-Streptomycin (100 U; Gibco) at 37 °C, 5% CO_2 and 95% humidity.

Human fallopian tube and tumor samples

The cases in this study were recruited under the Gynecological Oncology Targeted Therapy Study 01 (GO-Target-01, research ethics approval #11-SC-0014), the Oxford Radcliffe Biobank (ORB, research ethics approval 09/H0606/5+5 and 19/SC/0173) and the Oxford Ovarian Cancer-Predict Chemotherapy Response Trial (OXO-PCR-01, research ethics approval #12-SC-0404). All participants involved in this study were appropriately informed and consented.

Fallopian tube (FT) biopsies for single-cell RNA-seq were collected from the distal end of fallopian tubes. In total, we collected FT samples from six patients with HGSOC, five patients with endometrial cancer and five patients without cancer conditions (Table S1). Tumor samples were biopsied during diagnostic laparoscopy, immediately frozen on dry ice and stored in clearly labelled cryovials in -80 °C freezers.

METHOD DETAILS

Sample dissociation

The fallopian tube samples were processed in 1 hr, after being collected from the hospital. The tissues were dissociated with Human Tumor Dissociated kit (Miltenyi Biotec) and filtered using 100 µm SmarterStrainers (Miltenyi Biotec).

Culture, cryopreservation and harvest

Certain samples were cultured or cryopreserved in this study (Table S1). To culture primary cells from patients, we adopted the medium for FTE culturing (Kessler et al., 2015) (41.7 ml Advanced DMEM/F12 Medium, 540 µl HEPES, 450 µl P/S, 4.5 µl (10 ng/ml) EGF, 2.25 ml FBS (5%), 45 µl (9 µM) Rock inhibitor/Y0503-5MG, Y-27632 dihydrochloride Sigma-Aldrich, termed as FT culturing medium). Immediately after dissociation, cells were transferred into a 6-well plate for primary cell culture with the FT culturing medium at 37 °C in a CO_2 cell incubator, where they were cultured for overnight or long-term (LT, 2 days or 6 days).

For cryopreservation, cells were suspended in 1ml Synth-a-Freeze Cryopreservation Medium (Thermo Fisher). Cell suspension was frozen in freezing containers (Thermo Fisher) with Isopropyl alcohol at -80 °C for 24 hr before being transferred into liquid nitrogen. The cryopreservation cells were frozen down immediately after dissociation, stored in liquid nitrogen and recovered in FT culturing medium overnight after thawing. We were not able to generate cDNA from single cells that were immediately thawed from liquid nitrogen. Therefore, the frozen cells were recovered overnight in the FT culturing medium before cell sorting.

For cultured cells, cells were harvested with TrypLE (Thermo Fisher) for 5 min at 37 °C and dispensed in FACS buffer (1× PBS, 1% BSA, 2 mM EDTA, 0.0025% RNasin plus), and then they were processed as for the freshly dissociated cells.

Organoid culture

The three-dimensional organoid cultures were conducted as previously described (Kessler et al., 2015). The FT tissue was cut into small pieces of around 2-4 mm in length and incubated

in pre-warmed Digestive Medium containing Advanced DMEM/F12 (Gibco), 12 mM HEPES (Gibco), 1% Penicillin/Streptomycin (Gibco), 2 mg/ml Trypsin (Sigma), 0.5 mg/ml DNase I (Sigma) and 100 U/ml Collagenase Type I (Invitrogen); this was incubated for 45 min in rotation at 37 °C. Using forceps, decellularized tissue was removed and immediately filtered through a 100 µm cell strainer and pelleted by centrifugation at 300×g for 10 min. The cell pellet was washed once with ice-cold DPBS and resuspended in Matrigel Matrix (Corning). Using an 8-well chamber slide (Thistle Scientific), 20 µl of Matrigel were placed into each well by drops and the mixture was incubated at 37 °C for 20 min to allow Matrigel polymerizing and solidifying. Finally, cells were overlaid with pre-warmed organoid medium containing Advanced DMEM/F12, 12 mM HEPES, 1% Penecillin/Streptomycin, 1% N2 Supplement (Thermo Fisher), 2% B-27 Supplement (Thermo Fisher), 100 ng/ml human Noggin (Peprotech), 100 ng/ml human FGF10 (Peprotech), 1 mM Nicotinamide (Sigma), 0.5 µM TGF-b R Kinase Inhibitor VI (SB431542; ThermoFisher), R-Spondin1 protein (RSPO1) and 25% Wnt3a conditioned medium (ATCC). RSPO1 protein was produced in-house using a HA-RSPO1-Fc 293T cell line (Cultrex). Protein expression was performed according to Culturex protocol while protein purification was done using Pierce Protein A Agarose kit (ThermoFisher Scientific).

Cell sorting

To sort freshly dissociated cells or harvested cells, the cells were dispensed in the FACS buffer (1× PBS, 1% BSA, 2 mM EDTA, 0.0025% RNasin plus) and stained with EpCAM-APC antibody (Miltenyi Biotec) and CD45-FITC antibody (BioLegend) for 30 min at 4 °C in the dark. Afterwards, cells were washed once with FACS buffer and kept on ice in the dark. 10 µg/µl DAPI was added 10 min before cell sorting with SH800 sorter (Sony). The alive $EpCAM^{+}CD45^{-}DAPI^{-}$ fallopian tube epithelial cells were sorted into 96-well plates with one cell per well. Each batch was sorted with bulk controls (10 or 100 cells) and empty controls. A

small number of $EpCAM^-CD45^-DAPI^-$ or $EpCAM^-CD45^+DAPI^-$ cells were sorted as control for epithelial cells. The cells were sorted into 4 µl lysis buffer with 0.1 µl RNase inhibitor (Clontech), 1.9 µl 0.4% Triton X-100, 1 µl 10 µM 5`-biotinylated oligo-$dT_{30}VN$ (IDT) and 1 µl 10 mM dNTP (Thermo Scientific), snap frozen on dry ice and stored at -80 °C before single-cell RNA sequencing.

cDNA synthesis and library construction

The SMART-seq2 protocol (Picelli et al., 2014) was used to generate single-cell cDNA and libraries with optimization and automation. To lyse the cells, the aforementioned lysis buffer with single cells were removed from -80 °C, heated at 72 °C for 3min and then kept at 4 °C before adding the reverse transcription master mix. The reverse transcription step exactly followed SMART-seq2 protocol with 5'-biotinylated TSO (Qiagen). The first round of 24-cycle PCR started with 10 µl reverse transcription product, 0.125 µl 10 µM 5'-Biotinylated ISPCR primers (IDT), 12.5 µl KAPA HIFI PCR Master Mix (Roche Diagnostics) and 2.375 µl RT-PCR grade water (Invitrogen). PCR products were cleaned up with 0.8:1 Ampure XP beads (Beckman Coulter) with Biomek FxP Laboratory Automation Workstation (Biomek).

The quality of single-cell cDNA was checked on TapeStation with HD5000 Tapes and reagent (Agilent) and single-cell qPCR of *GAPDH* or *ACTB* with QuantiNova SYBR Green PCR Kit (Qiagen). The concentration was measured with Quant-iT™ PicoGreen™ dsDNA Assay Kit (Invitrogen) on the CLARIOstar Plate Reader (BMG Labtech). The wells where Ct values of *GAPDH* or *ACTB* were less than 20 were defined as the wells with good-quality cDNA. Good-quality cDNA was cherry-picked and normalized to 2 µg/ml with EB (Qiagen) on the Biomek FxP Workstation into a new 384-well plate (4titude).

We used the miniaturized Nextera XT (Illumina) protocol (Mora-Castilla et al., 2016) with Mosquito HTS (ttplabtech) to generate libraries from normalized single-cell cDNA in a 384-well Endure plate (Life Technology) with 400 nl input cDNA per reaction. The Nextera index

set A and D were used in parallel to multiplex 384 cells per batch. All 384 single-cell libraries in each batch were pooled and cleaned up with 0.6:1 Ampure XP beads (Beckman Coulter). The multiplexed RNA-seq library was normalized to 4nM with Suspension Buffer (provided in Nextera XT kit) to be sequenced on the NextSeq 500 Sequencer (Illumina).

Whole-exome sequencing

The buffy samples and tumor biopsies were stored at -80 °C. Tumor biopsies were frozen in the O.C.T. Compound (Fisher Scientific) and sectioned into 1.5 mL tubes for DNA extraction. The tumor sites were confirmed by H&E staining. Genomic DNA (gDNA) was extracted from buffy and tumor samples with the DNeasy Blood & Tissue Kits (Qiagen). The whole-exome sequencing libraries were prepared with the SureSelect Low Input Target Enrichment System (Agilent) and sequenced pair-ended on Illumina HiSeq. The reads were filtered with Trim Galore!, and mapped with Bowtie2 (Langmead and Salzberg, 2012). The somatic mutations were called via Platypus (Rimmer et al., 2014) and VarScan2 (Koboldt et al., 2013), and then analyzed by R package VariantAnnotation (Obenchain et al., 2014).

Laser capture microdissection

Tissue sectioning, H&E staining and the assessment by a gynecological oncology pathologist were performed as previously described (Hellner et al., 2016). Tissue biopsies were frozen down with Fisher Healthcare™ Tissue-Plus O.C.T. Compound (NEG-50, Richard-Allan Scientific) and sectioned by 10 µm in CryoStar NX50 Cryostat (Thermo Scientific). The tissue sections were stored at -80 °C before proceeding with the staining step.

The pre-chemotherapy tumor biopsies were fresh frozen in OCT and sectioned onto polyethylene naphthalate membrane (PEN) glass slides (MembraneSlide 1.0 PEN, Zeiss) at 6 µm and immediately stored at -80 °C until the laser capture microdissection (LCM). Prior to LCM, the slides were taken out from -80 °C, immediately immerged in 70% ethanol for 2 min, in Cresyl Violet (Sigma Aldrich) for 2 min, rinsed in 95% ethanol five times to remove residual

cresyl violet and dried at room temperature for 2 min.

LCM was conducted on the PALM Laser Microdissection System (Zeiss) and the captured cells were collected onto the adhesive caps of PCR tubes (AdhesiveCap 500 opaque, Zeiss), then immediately resuspended in 10 µl lysis buffer (RNAqueous™-Micro Total RNA Isolation Kit, Invitrogen). RNA was extracted according to the manufacturer's instructions and 3 µl of eluate before DNase treatment was kept for Whole Genome Amplification and stored at -20 °C. The remaining RNA was DNase treated, assessed with the Agilent TapeStation 2200 (Agilent) and then stored at -80 °C.

Bulk RNA sequencing

The SMARTer Stranded Total RNA-Seq kit v2 - Pico Input (Takara) was used to prepare sequencing libraries which were indexed, enriched by 15 cycles of amplification, assessed using the Agilent TapeStation and then quantified by Qubit. Multiplexed library pools were quantified with the KAPA Library Quantification Kit (KK4835) and sequenced using 75 bp pair end reads on the Illumina NextSeq500 platform. Fastq files were trimmed for adapter sequences and quality. Trimmed reads were then mapped to the human hg19 reference genome using STAR (v2.4.2a) and read counts were obtained using subread FeatureCounts (v1.4.5-p1).

Immunofluorescent staining

To do immunofluorescent staining on the frozen OCT-embedded tissue sections, slides were taken out from -80 °C and thawed at room temperature for 5 min. The slides were washed with ice-cold PBS twice to remove the OCT and then fixed in ice-cold 4% PFA for 10 min. The fixed slides were washed with PBS/Glycine buffer to remove residual PFA and then permeabilized with Permeabilization Buffer (1× PBS, 0.5% Triton X-100) for 10 min at RT. A hydrophobic circle was drawn around the tissue region with the PAP pen (Abcam) and dried for 5 min at room temperature (RT). The permeabilized slides were washed in Wash Buffer (1× PBS, 0.2% Triton X-100, 0.05% Tween-20) and blocked in Blocking Buffer (Wash buffer, 10%

donkey serum, Sigma) for 1-2 hr. The diluted primary antibodies were incubated at 4 °C overnight or at RT for 1-2 hr. The slides were washed and incubated with the secondary antibodies (1:200) and DAPI (1:1000) at RT for 1-2 hr. The stained slides were washed, mounted with the mounting medium without DAPI (Vector Laboratories) and covered. Then they were dried for 1-2 hr at RT in dark before being imaged using a confocal microscope (Zeiss 780). The samples used for staining are listed in Table S1.

Immunohistochemistry

The Formalin-Fixed Paraffin-Embedded (FFPE) samples were sectioned into 2.5 or 4 μm. We used the Leica Bond Max autostainer (Leica Microsystems) or Autostainer plus Link 48 (Dako) to automatically stain the tissue sections. The standard Heat Induced Epitope Retrieval (HIER) in retrieval buffer pH 6 was used. Tissue sections were kept at 100 °C for 20 min and incubated with the primary antibody or lgG control for up to 1 hr. We used the Aperio slide scanner (Aperio) to scan the stained slides at 20× or 40× magnification. The samples used for staining are listed in Table S1.

QUANTIFICATION AND STATISTICAL ANALYSIS

Preprocessing scRNA-seq data

Sequencing files were trimmed by Trim Galore!, mapped to UCSC hg19 human genome assembly by STAR (Dobin et al., 2012) and counted by FeatureCount (Liao et al., 2014). The quality of the expression data was checked by the R package scater (McCarthy et al., 2017) and the low-quality cells were filtered out from further analysis. We used three criteria to filter cells for further analysis: first, the number of genes detected per cells was more than 1200 and less than 7500; second, the total number of read counts was more than 0.1 million per cell; third, the percentage of counts of the top highly expressed 200 genes was less than 85% to ensure enough complexity of the transcriptomes. The upper cutoff for numbers of genes per

cells was aimed to filter out the putative doublets. After filtering, the numbers of detected genes per cell were between 1,202 and 7,496 (mean: 3,665). The numbers of total reads per cell were between 102,319 and 9,668,129 (mean: 763,233).

Detecting doublets

To effectively detect doublets, we used R package DoubletFinder (McGinnis et al., 2019). In brief, we combined all fresh cells (secretory cells, ciliated cells, fibroblasts and leukocytes), constructed a Seurat S4 object (Butler et al., 2018) and ran DoubletFinder with its default pipeline.

Visualization of expression data

The uniform manifold approximation and projection (UMAP) plots were based on the functions of runUMAP and plotUMAP, and the violin plots of expression were plotted by the function plotExpression from the R package scater. Heatmaps were plotted by R packages pheatmap and ggplot2 (Ginestet, 2011).

Comparing fresh and cultured cells

To investigate the effects of cell culture, we first combined secretory cells from Patient 11553 and Patient 15072. Then we used limma-voom to identify the DE genes in three pairs of comparisons, namely fresh versus overnight, fresh versus LT and overnight versus LT. The threshold of DE genes was fold-change ≥ 2 and FDR < 0.05. The total number of DE genes affected by culture condition was 4061. The GO analysis was conducted by Gorilla with cutoffs at FDR < 0.05.

Pseudotime analysis

We used the R package PhenoPath (Campbell and Yau, 2018) to perform the pseudotime analysis that projected the high-dimensional transcriptomic data to one dimension, in which we compared fresh, overnight cultured and long-term cultured cells. The expression matrix that was normalized by the R package scater was used as the input and the first principal component

was used as the initialization of the latent trajectory to accelerate the convergence.

Filtering to select fresh secretory cells

Only the cells that belonged to the secretory cluster and the fresh group were kept expect for the cells from the 15066-left tube (15066L), because the cells from 15066L formed a patient-specific cluster (Figure 1F) and it was reported to have salpingitis on this side. Secretory cells with strong expression of *KRT7* and *EPCAM* (log [CPM+1] > 2), no expression for *PTPRC* (log [CPM+1] = 0) or *CCDC17* (log [CPM+1] < 1) and no observed copy number variants were kept for the clustering analysis. Copy number variants were detected by HoneyBADGER with default settings (Fan et al., 2018).

Single-nucleotide variants (SNVs) were called from piled up BAM files by MonoVar (Li et al., 2009; Zafar et al., 2016) with the recommended parameters (samtools mpileup -BQ0 -d10000 -f ref.fa -q 40 -b filenames.txt | monovar.py -p 0.002 -a 0.2 -t 0.05 -m 2 -f ref.fa -b filenames.txt -o output.vcf). SNVs in exome regions were intersected by the Bedtools (Quinlan and Hall, 2010).

Differentially-expressed-based clustering

We used an in-house clustering algorithm to identify the cell populations across patients. In brief, the clustering method contained three steps: (1) an initial clustering step within the individual patients by Spectral Clustering (Karatzoglou et al., 2004; Ng et al., 2002); (2) calculation of distance between each pair of initial clusters by differential expression (DE) analysis; (3) a final hierarchical clustering across different patients based on the calculated distance matrix (Figure 1B).

The clustering approach for clinical scRNA-seq data required the input of an expression matrix, where the rows corresponded to genes/features and the columns corresponded to cells. The patient source of all cells was denoted by a vector. The length of this source vector was equal to number of cells and the number of different values in the source vector was equal to

the number of patients. For the dataset containing multiple patients, our method consisted of three main steps.

The count matrix was preprocessed by log-normalization, selection of high variance genes (Satija et al., 2015), centered and dimensionally reduced by the principal component analysis. The first step was initial clustering of the cells within individual patients by the weighted k-nearest neighbors spectral clustering provided by kknn (Hechenbichler and Schliep, 2004). After spectral clustering, each cell was assigned to a patient-specific initial cluster. Cells from different patients were clustered into separate patient-specific clusters.

The second step was pairwise differential expression (DE) analysis by limma voom (Law et al., 2014; Phipson et al., 2016; Ritchie et al., 2015) between initial clusters across patients to build a distance matrix, because it was reported to be one of the top ranking DE analysis methods for scRNA-seq (Soneson and Robinson, 2018). There were two modes to calculate the distance. The first one was unweighted, meaning that the distance between two initial clusters was defined as the number of differentially expressed genes (DEGs) between them. The second mode was weighted. The DE genes had different weights in the distance. The DE genes with higher fold change and larger ratio of expression had higher weight. The weighted method had advantages in identifying rare but functionally distinguished cell types. As a result, a distance matrix of functional dissimilarity was constructed among all initial clusters.

In the last step, all initial clusters were assigned to the final clusters by hierarchical clustering based on the aforementioned distance matrix. Accordingly, the single cells were assigned to the final cluster containing the initial cluster that the cells belong to. The hierarchical tree was plotted to help dividing the final clusters.

Data integration

To validate the discovered secretory subtypes in the samples from benign patients, we used the data integration from Seurat v3 (Stuart et al., 2019). The integration step merged the high-

quality fresh secretory cells from five cancer patients and five benign patients. The cells were first split by their batches. We normalized the count matrix by the vst method and selected the top 1000 high variance genes by using Seurat. Then we computed the integration anchors by using the first 10 dimensions and set the number of k nearest neighbors for finding anchors as 5 (other parameters were default), and then we merged the data by using the computed anchors.

Identifying marker genes

The identification of markers was based on limma-voom, which has good performance with scRNA-seq data (Soneson and Robinson, 2018). To spot the positive markers in the target cluster, we conducted the differential expression analysis between the target cluster and background (non-target) clusters. Only if one gene emerged in all the pairwise comparisons between the target cluster and background clusters with FDR < 0.05 and $\log_2$ fold-change > 0.4, this gene was defined as the marker gene of this target cluster.

Gene ontology enrichment analysis

Gene ontology enrichment analysis was conducted on GOrilla (last updated on May 26, 2018) (Eden et al., 2007; 2009). The statistical overrepresentation was conducted by the PANTHER Gene list analysis (Thomas, 2003). Pathway enrichment analysis was done by the DAVID Bioinformatics Resources 6.8 (Huang et al., 2009b; 2009a). The threshold of significance was FDR < 0.05.

Bulk expression data

TCGA data was downloaded from the UCSC Xena Data Hub (https://tcga.xenahubs.net) (Goldman et al., 2018) and the Broad firehose (https://gdac.broadinstitute.org), which was derived from the TCGA Data Coordinating Centre (version: Jan 2016). We used the "IlluminaHiSeq UNC" RNA-seq dataset (version: 2017-10-13) and the "TCGA OV gene expression subtype" phenotype data (version: 2016-05-27). The AOCS dataset was downloaded from GSE9899. The other microarray datasets were retrieved from the R package

CuratedOvarianData (Ganzfried et al., 2013).

Deconvolution of bulk expression data

On the basis of our FTE scRNA-seq data, we firstly selected the marker genes for five FTE subtypes, namely Differentiated (C3), KRT17 cluster (C4), Cell cycle (C9), EMT (C7) and Ciliated signatures by using the following cutoffs: (1) $\log_2$ fold-change ≥ 1.5; (2) FDR ≤ 0.01; (3) dispersion ≥ 0.2 that was measured by the variable loadings in the principal component analysis of TCGA RNA-seq data; (4) the correlation with each other markers was less than 0.9 in TCGA data to avoid redundancy. We calculated the reference matrix (Figure 5A and Table S7) by BSEQ-sc (Baron et al., 2016) that measured that average expression levels of marker genes in each cell subtype. We used this reference matrix to deconvolute the RNA-seq data from TCGA, the microarray data from AOCS and CuratedOvarianData and the OXO-PCR RNA-seq data by CIBERSORT as previously described (Newman et al., 2015), which is based on the u-parameter support vector regression and is robust to noise and outliers. The CIBERSORT was ran in the relative mode with non-logged expression matrices. For the microarray data, if a gene corresponded to multiple probes, we selected the probe that had the highest average expression level to represent that gene. The deconvolution analysis generated scores of the five transcriptomic signatures in each tumor sample (Figure 5A). This score of a signature can be interpreted as the proportion of the corresponding cell state in a tumor sample.

Survival analysis

The survival analysis was conducted by fitting a Cox proportional hazards regression model. This analysis used age, grade and residual disease as covariates. We repeated the survival analysis in TCGA RNA-seq dataset, AOCS microarray dataset and other seven microarray datasets from the CuratedOvarianData database (Ganzfried et al., 2013). The criterion of selecting datasets was that a dataset contained over one hundred clinical samples. We filtered out the non-serous cases. The following analysis was performed on SOC cases only. For the

datasets from CuratedOvarianData that contained both low and high grades or early and late stages, we used the multivariate analysis to eliminate the effects of confounding factors. In the multi-variate survival analysis, we dichotomized grades to low-grade (Grade 1) and high-grade (Grades 2 and 3) and dichotomized stages to early (Stages I and II) and late (Stages III and IV) (Table S9). EMT scores and overall survival were negatively correlated in the independent eight datasets ($P < 0.05$), except for the "GSE32062.GPL6480" dataset (see Table 1). The hazard ratios of EMT scores in all the nine independent datasets were larger than 1 (range: 1.88 – 3.31). For the survival curve of the meta-analysis (Figure 6C), we dichotomized the EMT-low and EMT-high groups by the median of EMT scores of each dataset to avoid batch effects.

Data and code availability

The code generated during this study are available at GitHub (web link: https://github.com/zhiyhu/scFT-paper). Single-cell RNA sequencing datasets of fallopian tubes from cancer and benign patients are deposited at Gene Expression Omnibus (GEO accession numbers: GSE132149 and GSE139079, respectively). The bulk RNA sequencing dataset is deposited at Gene Expression Omnibus (GEO accession number: GSE132107).

Supplementary Video

Video S1, related to Figure 6. Z-stack of IF staining shows the pan-cytokeratin and SPARC double positive cells in HGSOC.

Excel table title and legends

Table S1, related to Figure 1. Patient information of GO-TARGET subjects.

Table S2, related to Figure 1. Results of gene ontology enrichment analysis (GOEA) between fresh and overnight-cultured cells.

Table S3, related to Figure 1. List of differentially expressed (DE) genes between fresh and overnight-cultured cells.

Table S4, related to Figure 2. List of markers of secretory and ciliated cells.

Table S6, related to Figure 2. List of marker genes of secretory subtypes.

Table S7, related to Figure 5. Reference matrix for deconvolution.

Table S8, related to Figure 5. List of marker genes and miRNAs of EMT-high tumors.

References

Ahmed, A.A., Etemadmoghadam, D., Temple, J., Lynch, A.G., Riad, M., Sharma, R., Stewart, C., Fereday, S., Caldas, C., DeFazio, A., et al. (2010). Driver mutations in TP53 are ubiquitous in high grade serous carcinoma of the ovary. J. Pathol. *221*, 49–56.

Anastassiou, D., Rumjantseva, V., Cheng, W., Huang, J., Canoll, P.D., Yamashiro, D.J., and Kandel, J.J. (2011). Human cancer cells express Slug-based epithelial-mesenchymal transition gene expression signature obtained in vivo. BMC Cancer *11*, 529.

Anglesio, M.S., Wiegand, K.C., Melnyk, N., Chow, C., Salamanca, C., Prentice, L.M., Senz, J., Yang, W., Spillman, M.A., Cochrane, D.R., et al. (2013). Type-specific cell line models for type-specific ovarian cancer research. PLoS ONE *8*, e72162.

Ansieau, S., Bastid, J., Doreau, A., Morel, A.-P., Bouchet, B.P., Thomas, C., Fauvet, F., Puisieux, I., Doglioni, C., Piccinin, S., et al. (2008). Induction of EMT by twist proteins as a collateral effect of tumor-promoting inactivation of premature senescence. Cancer Cell *14*, 79–89.

Ardighieri, L., Lonardi, S., Moratto, D., Facchetti, F., Shih, I.-M., Vermi, W., and Kurman, R.J. (2014). Characterization of the immune cell repertoire in the normal fallopian tube. Int. J. Gynecol. Pathol. *33*, 581–591.

Baron, M., Veres, A., Wolock, S.L., Faust, A.L., Gaujoux, R., Vetere, A., Ryu, J.H., Wagner, B.K., Shen-Orr, S.S., Klein, A.M., et al. (2016). A Single-Cell Transcriptomic Map of the Human and Mouse Pancreas Reveals Inter- and Intra-cell Population Structure. Cell Syst *3*, 346–.

Bell, D., Berchuck, A., Birrer, M., Chien, J., Cramer, D.W., Dao, F., Dhir, R., DiSaia, P., Gabra, H., Glenn, P., et al. (2011). Integrated genomic analyses of ovarian carcinoma. Nature *474*, 609–615.

Bentink, S., Haibe-Kains, B., Risch, T., Fan, J.B., Hirsch, M.S., Holton, K., Rubio, R., April, C., Chen, J., Wickham-Garcia, E., et al. (2012). Angiogenic mRNA and microRNA gene expression signature predicts a novel subtype of serous ovarian cancer. PLoS ONE *7*, e30269.

Bertucci, F., Finetti, P., and Birnbaum, D. (2012). Basal Breast Cancer: A Complex and Deadly Molecular Subtype. Curr. Mol. Med. *12*, 96–110.

Biton, M., Haber, A.L., Rogel, N., Burgin, G., Beyaz, S., Schnell, A., Ashenberg, O., Su, C.-W., Smillie, C., Shekhar, K., et al. (2018). T Helper Cell Cytokines Modulate Intestinal Stem Cell Renewal and Differentiation. Cell *175*, 1307–1320.e1322.

Bonome, T., Levine, D.A., Shih, J., Randonovich, M., Pise-Masison, C.A., Bogomolniy, F., Ozbun, L., Brady, J., Barrett, J.C., Boyd, J., et al. (2008). A gene signature predicting for survival in suboptimally debulked patients with ovarian cancer. Cancer Res. *68*, 5478–5486.

Brock, A., Chang, H., and Huang, S. (2009). Non-genetic heterogeneity--a mutation-independent driving force for the somatic evolution of tumours. Nature Reviews Genetics *10*, 336–342.

Butler, A., Hoffman, P., Hoffman, P., Smibert, P., Smibert, P., Papalexi, E., Papalexi, E., and Satija, R. (2018). Integrating single-cell transcriptomic data across different conditions, technologies, and species. Nature Biotechnology *36*, 411–420.

Campbell, K.R., and Yau, C. (2018). Uncovering pseudotemporal trajectories with covariates from single cell and bulk expression data. Nat Commun *9*.

Cerny, K.L., Ribeiro, R.A.C., Jeoung, M., Ko, C., and Bridges, P.J. (2016). Estrogen Receptor Alpha (ESR1)-Dependent Regulation of the Mouse Oviductal Transcriptome. PLoS ONE *11*, e0147685.

Chandrasekaran, K.S., Sathyanarayanan, A., and Karunagaran, D. (2016). MicroRNA-214 suppresses growth, migration and invasion through a novel target, high mobility group AT-hook 1, in human cervical and colorectal cancer cells. Br. J. Cancer *115*, 741–751.

Chen, G.M., Kannan, L., Geistlinger, L., Kofia, V., Safikhani, Z., Gendoo, D.M.A., Parmigiani, G., Birrer, M., Haibe-Kains, B., and Waldron, L. (2018). Consensus on Molecular Subtypes of High-Grade Serous Ovarian Carcinoma. Clin. Cancer Res. *24*, 5037–5047.

Clyman, M.J. (1966). Electron microscopy of the human fallopian tube. Fertil. Steril. *17*, 281–301.

Comer, M.T., Leese, H.J., and Southgate, J. (1998). Induction of a differentiated ciliated cell phenotype in primary cultures of Fallopian tube epithelium. Human Reproduction *13*, 3114–3120.

Crijns, A.P.G., Fehrmann, R.S.N., de Jong, S., Gerbens, F., Meersma, G.J., Klip, H.G., Hollema, H., Hofstra, R.M.W., Meerman, te, G.J., de Vries, E.G.E., et al. (2009). Survival-related profile, pathways, and transcription factors in ovarian cancer. PLoS Med. *6*, e24.

CROW, J., AMSO, N.N., LEWIN, J., and SHAW, R.W. (1994). Morphology and Ultrastructure of Fallopian-Tube Epithelium at Different Stages of the Menstrual-Cycle and Menopause. Human Reproduction *9*, 2224–2233.

Dai, X., Li, T., Bai, Z., Yang, Y., Liu, X., Zhan, J., and Shi, B. (2015). Breast cancer intrinsic subtype classification, clinical use and future trends. Am J Cancer Res *5*, 2929–2943.

Davis, F.M., Stewart, T.A., Thompson, E.W., and Monteith, G.R. (2014). Targeting EMT in cancer: opportunities for pharmacological intervention. Trends Pharmacol. Sci. *35*, 479–488.

Dobin, A., Davis, C.A., Schlesinger, F., Drenkow, J., Zaleski, C., Jha, S., Batut, P., Chaisson, M., and Gingeras, T.R. (2012). STAR: ultrafast universal RNA-seq aligner. Bioinformatics *29*, 15–21.

Domcke, S., Sinha, R., Levine, D.A., Sander, C., and Schultz, N. (2013). Evaluating cell lines as tumour models by comparison of genomic profiles. Nat Commun *4*, 2126.

Ducie, J., Dao, F., Considine, M., Olvera, N., Shaw, P.A., Kurman, R.J., Shih, I.-M., Soslow, R.A., Cope, L., and Levine, D.A. (2017). Molecular analysis of high-grade serous ovarian carcinoma with and without associated serous tubal intra-epithelial carcinoma. Nat Commun *8*, 990.

Eckert, M.A., Coscia, F., Chryplewicz, A., Chang, J.W., Hernandez, K.M., Pan, S., Tienda, S.M., Nahotko, D.A., Li, G., Blaženović, I., et al. (2019). Proteomics reveals NNMT as a master metabolic regulator of cancer-associated fibroblasts. Nature *474*, 609–728.

Eden, E., Lipson, D., Yogev, S., and Yakhini, Z. (2007). Discovering motifs in ranked lists of DNA sequences. PLoS Comput Biol *3*, 508–522.

Eden, E., Navon, R., Steinfeld, I., Lipson, D., and Yakhini, Z. (2009). GOrilla: a tool for discovery and visualization of enriched GO terms in ranked gene lists. BMC Bioinformatics *10*.

Etemadmoghadam, D., DeFazio, A., Beroukhim, R., Mermel, C., George, J., Getz, G., Tothill, R., Okamoto, A., Raeder, M.B., Harnett, P., et al. (2009). Integrated genome-wide DNA copy number and expression analysis identifies distinct mechanisms of primary chemoresistance in ovarian carcinomas. Clin. Cancer Res. *15*, 1417–1427.

Fan, J., Lee, H.-O., Lee, S., Ryu, D.-E., Lee, S., Xue, C., Kim, S.J., Kim, K., Barkas, N., Park, P.J., et al. (2018). Linking transcriptional and genetic tumor heterogeneity through allele analysis of single-cell RNA-seq data. Genome Res. gr.228080.117.

Fessler, E., and Medema, J.P. (2016). Colorectal Cancer Subtypes: Developmental Origin and Microenvironmental Regulation. Trends Cancer *2*, 505–518.

Ford, C.E., Jary, E., Ma, S.S.Q., Nixdorf, S., Heinzelmann-Schwarz, V.A., and Ward, R.L. (2013). The Wnt gatekeeper SFRP4 modulates EMT, cell migration and downstream Wnt signalling in serous ovarian cancer cells. PLoS ONE *8*, e54362.

Fresno Vara, J.A., Casado, E., de Castro, J., Cejas, P., Belda-Iniesta, C., and González-Barón, M. (2004). PI3K/Akt signalling pathway and cancer. Cancer Treat. Rev. *30*, 193–204.

Ganzfried, B.F., Riester, M., Haibe-Kains, B., Risch, T., Tyekucheva, S., Jazic, I., Wang, X.V., Ahmadifar, M., Birrer, M.J., Parmigiani, G., et al. (2013). curatedOvarianData: clinically annotated data for the ovarian cancer transcriptome. Database (Oxford) *2013*, bat013.

Ghosh, A., Syed, S.M., and Tanwar, P.S. (2017). In vivo genetic cell lineage tracing reveals that oviductal secretory cells self-renew and give rise to ciliated cells. *144*, 3031–3041.

Gilbertson, R.J. (2011). Mapping cancer origins. Cell *145*, 25–29.

Ginestet, C. (2011). ggplot2: Elegant Graphics for Data Analysis. Journal of the Royal Statistical Society Series a-Statistics in Society *174*, 245–245.

Ginestier, C., Hur, M.H., Charafe-Jauffret, E., Monville, F., Dutcher, J., Brown, M., Jacquemier, J., Viens, P., Kleer, C.G., Liu, S., et al. (2007). ALDH1 is a marker of normal and malignant human mammary stem cells and a predictor of poor clinical outcome. Cell Stem Cell *1*, 555–567.

Goldman, M., Craft, B., Kamath, A., Brooks, A.N., Zhu, J., and Haussler, D. (2018). The UCSC Xena Platform for cancer genomics data visualization and interpretation. bioRxiv 326470. https://www.biorxiv.org/content/10.1101/326470v5

Greaves, M., and Maley, C.C. (2012). Clonal evolution in cancer. Nature *481*, 306–313.

Gregory, P.A., Bert, A.G., Paterson, E.L., Barry, S.C., Tsykin, A., Farshid, G., Vadas, M.A., Khew-Goodall, Y., and Goodall, G.J. (2008). The mir-200 family and mir-205 regulate epithelial to mesenchymal transition by targeting ZEB1 and SIP1. Nat. Cell Biol. *10*, 593–601.

Grün, D., Lyubimova, A., Kester, L., Wiebrands, K., Basak, O., Sasaki, N., Clevers, H., and van Oudenaarden, A. (2015). Single-cell messenger RNA sequencing reveals rare intestinal cell types. Nature *525*, 251–255.

Gupta, P.B., Fillmore, C.M., Jiang, G., Shapira, S.D., Tao, K., Kuperwasser, C., and Lander, E.S. (2011). Stochastic state transitions give rise to phenotypic equilibrium in populations of cancer cells. Cell *146*, 633–644.

Hanahan, D., and Weinberg, R.A. (2011). Hallmarks of Cancer: The Next Generation. Cell *144*, 646–674.

Hechenbichler K. and Schliep K.P. (2004) Weighted k-Nearest-Neighbor Techniques and Ordinal Classification, Discussion Paper 399, SFB 386, Ludwig-Maximilians University Munich

Hellner, K., Miranda, F., Fotso Chedom, D., Herrero-Gonzalez, S., Hayden, D.M., Tearle, R., Artibani, M., KaramiNejadRanjbar, M., Williams, R., Gaitskell, K., et al. (2016). Premalignant SOX2 overexpression in the fallopian tubes of ovarian cancer patients: Discovery and validation studies. Ebiom *10*, 137–149.

Honkaniemi, J., Kainu, T., Ceccatelli, S., Rechardt, L., Hökfelt, T., and Pelto-Huikko, M. (1992). Fos and jun in rat central amygdaloid nucleus and paraventricular nucleus after stress. Neuroreport *3*, 849–852.

Huang, D.W., Sherman, B.T., and Lempicki, R.A. (2009a). Systematic and integrative analysis of large gene lists using DAVID bioinformatics resources. Nature Protocols *4*, 44–57.

Huang, D.W., Sherman, B.T., and Lempicki, R.A. (2009b). Bioinformatics enrichment tools: paths toward the comprehensive functional analysis of large gene lists. Nucleic Acids Research *37*, 1–13.

Ince, T.A., Richardson, A.L., Bell, G.W., Saitoh, M., Godar, S., Karnoub, A.E., Iglehart, J.D., and Weinberg, R.A. (2007). Transformation of different human breast epithelial cell types leads to distinct tumor phenotypes. Cancer Cell *12*, 160–170.

Ince, T.A., Sousa, A.D., Jones, M.A., Harrell, J.C., Agoston, E.S., Krohn, M., Selfors, L.M., Liu, W., Chen, K., Yong, M., et al. (2015). Characterization of twenty-five ovarian tumour cell lines that phenocopy primary tumours. Nat Commun *6*, 7419.

Ishay-Ronen, D., Diepenbruck, M., Kalathur, R.K.R., Sugiyama, N., Tiede, S., Ivanek, R., Bantug, G., Morini, M.F., Wang, J., Hess, C., et al. (2019). Gain Fat-Lose Metastasis: Converting Invasive Breast Cancer Cells into Adipocytes Inhibits Cancer Metastasis. Cancer Cell *35*, 17–32.e6.

Jiang, Y.-P., Wu, X.-H., Shi, B., Wu, W.-X., and Yin, G.-R. (2006). Expression of chemokine CXCL12 and its receptor CXCR4 in human epithelial ovarian cancer: an independent prognostic factor for tumor progression. Gynecol. Oncol. *103*, 226–233.

Kang, Y., and Massagué, J. (2004). Epithelial-mesenchymal transitions: twist in development and metastasis. Cell *118*, 277–279.

Karatzoglou, A., Smola, A., Hornik, K., and Zeileis, A. (2004). kernlab- An S4Package for Kernel Methods in R. J Stat Softw *11*, 1–20.

Karlan, B.Y., Dering, J., Walsh, C., Orsulic, S., Lester, J., Anderson, L.A., Ginther, C.L., Fejzo, M., and Slamon, D. (2014). POSTN/TGFBI-associated stromal signature predicts poor prognosis in serous epithelial ovarian cancer. Gynecol. Oncol. *132*, 334–342.

Kessler, M., Hoffmann, K., Brinkmann, V., Thieck, O., Jackisch, S., Toelle, B., Berger, H., Mollenkopf, H.-J., Mangler, M., Sehouli, J., et al. (2015). The Notch and Wnt pathways regulate stemness and differentiation in human fallopian tube organoids. Nat Commun *6*, 8989.

Kim, J., Coffey, D.M., Creighton, C.J., Yu, Z., Hawkins, S.M., and Matzuk, M.M. (2012). High-grade serous ovarian cancer arises from fallopian tube in a mouse model. Proc. Natl. Acad. Sci. U.S.a. *109*, 3921–3926.

Klein, A.M., Mazutis, L., Akartuna, I., Tallapragada, N., Veres, A., Li, V., Peshkin, L., Weitz, D.A., and Kirschner, M.W. (2015). Droplet barcoding for single-cell transcriptomics applied to embryonic stem cells. Cell *161*, 1187–1201.

Klos Dehring, D.A., Vladar, E.K., Werner, M.E., Mitchell, J.W., Hwang, P., and Mitchell, B.J. (2013). Deuterosome-mediated centriole biogenesis. Dev. Cell *27*, 103–112.

Koboldt, D.C., Larson, D.E., and Wilson, R.K. (2013). Using VarScan 2 for Germline Variant Calling and Somatic Mutation Detection. Curr Protoc Bioinformatics *44*, 15.4.1–.4.17.

Konecny, G.E., Wang, C., Hamidi, H., Winterhoff, B., Kalli, K.R., Dering, J., Ginther, C., Chen, H.-W., Dowdy, S., Cliby, W., et al. (2014). Prognostic and therapeutic relevance of molecular subtypes in high-grade serous ovarian cancer. J. Natl. Cancer Inst. *106*, 11.

Koshiyama, M., Matsumura, N., and Konishi, I. (2017). Subtypes of Ovarian Cancer and Ovarian Cancer Screening. Diagnostics (Basel) *7*, 12.

Kuhn, E., Kurman, R.J., Sehdev, A.S., and Shih, I.-M. (2012). Ki-67 Labeling Index as an Adjunct in the Diagnosis of Serous Tubal Intraepithelial Carcinoma. International Journal of Gynecological Pathology *31*, 416–422.

Labidi-Galy, S.I., Papp, E., Hallberg, D., Niknafs, N., Adleff, V., Noe, M., Bhattacharya, R., Novak, M., Jones, S., Phallen, J., et al. (2017). High grade serous ovarian carcinomas originate in the fallopian tube. Nat Commun *8*, 1093.

Langmead, B., and Salzberg, S.L. (2012). Fast gapped-read alignment with Bowtie 2. Nat Meth *9*, 357–359.

Law, C.W., Chen, Y., Shi, W., and Smyth, G.K. (2014). voom: precision weights unlock linear model analysis tools for RNA-seq read counts. Genome Biol. *15*.

Li, Y.-R., and Yang, W.-X. (2016). Myosins as fundamental components during tumorigenesis: diverse and indispensable. Oncotarget *7*, 46785–46812.

Liao, Y., Smyth, G.K., and Shi, W. (2014). featureCounts: an efficient general purpose program for assigning sequence reads to genomic features. Bioinformatics *30*, 923–930.

Liu, M., Roth, A., Yu, M., Morris, R., Bersani, F., Rivera, M.N., Lu, J., Shioda, T., Vasudevan, S., Ramaswamy, S., et al. (2013). The IGF2 intronic miR-483 selectively enhances transcription from IGF2 fetal promoters and enhances tumorigenesis. Genes Dev. *27*, 2543–2548.

Macintyre, G., Goranova, T.E., De Silva, D., Ennis, D., Piskorz, A.M., Eldridge, M., Sie, D., Lewsley, L.-A., Hanif, A., Wilson, C., et al. (2018). Copy number signatures and mutational processes in ovarian carcinoma. Nat Genet *45*, 1127–1270.

Macosko, E.Z., Basu, A., Satija, R., Nemesh, J., Shekhar, K., Goldman, M., Tirosh, I., Bialas, A.R., Kamitaki, N., Martersteck, E.M., et al. (2015). Highly Parallel Genome-wide Expression Profiling of Individual Cells Using Nanoliter Droplets. Cell *161*, 1202–1214.

Mahalingaiah, P.K.S., Ponnusamy, L., and Singh, K.P. (2015). Chronic Oxidative Stress Leads to Malignant Transformation Along With Acquisition of Stem Cell Characteristics, and Epithelial to Mesenchymal Transition in Human Renal Epithelial Cells. J. Cell. Physiol. *230*, 1916–1928.

Marusyk, A., Almendro, V., and Polyak, K. (2012). Intra-tumour heterogeneity: a looking glass for cancer? Nature Reviews Cancer *12*, 323–334.

Mateescu, B., Batista, L., Cardon, M., Gruosso, T., de Feraudy, Y., Mariani, O., Nicolas, A., Meyniel, J.-P., Cottu, P., Sastre-Garau, X., et al. (2011). miR-141 and miR-200a act on ovarian tumorigenesis by controlling oxidative stress response. Nat. Med. *17*, 1627–1635.

McCarthy, D.J., McCarthy, D.J., Campbell, K.R., Campbell, K.R., Lun, A.T.L., Wills, Q.F., and Wills, Q.F. (2017). Scater: pre-processing, quality control, normalization and visualization of single-cell RNA-seq data in R. Bioinformatics *33*, 1179–1186.

McGinnis, C.S., Murrow, L.M., and Gartner, Z.J. (2019). DoubletFinder: Doublet Detection in Single-Cell RNA Sequencing Data Using Artificial Nearest Neighbors. Cell Syst *8*, 329–337.e4.

McGranahan, N., and Swanton, C. (2017). Clonal Heterogeneity and Tumor Evolution: Past, Present, and the Future. Cell *168*, 613–628.

McLean, G.W., Carragher, N.O., Avizienyte, E., Evans, J., Brunton, V.G., and Frame, M.C. (2005). The role of focal-adhesion kinase in cancer - a new therapeutic opportunity. Nature Reviews Cancer *5*, 505–515.

Meacham, C.E., and Morrison, S.J. (2013). Tumour heterogeneity and cancer cell plasticity. Nature *501*, 328–337.

Mora-Castilla, S., To, C., Vaezeslami, S., Morey, R., Srinivasan, S., Dumdie, J.N., Cook-Andersen, H., Jenkins, J., and Laurent, L.C. (2016). Miniaturization Technologies for Efficient Single-Cell Library Preparation for Next-Generation Sequencing. J Lab Autom *21*, 557–567.

Nalepa, G., and Clapp, D.W. (2018). Fanconi anaemia and cancer: an intricate relationship. Nature Reviews Cancer *18*, 168–185.

Newman, A.M., Liu, C.L., Green, M.R., Gentles, A.J., Feng, W., Xu, Y., Hoang, C.D., Diehn, M., and Alizadeh, A.A. (2015). Robust enumeration of cell subsets from tissue expression profiles. Nat Meth *12*, 453–.

Ng, A., Jordan, M., and Weiss, Y. (2002). On Spectral Clustering: Analysis and an algorithm. NIPS'01 Proceedings of the 14th International Conference on Neural Information Processing Systems: Natural and Synthetic, pp. 849-856

Nieto, M.A., Huang, R.Y.-J., Jackson, R.A., and Thiery, J.P. (2016). EMT: 2016. Cell *166*, 21–45.

Nowell, P.C. (1976). The clonal evolution of tumor cell populations. Science *194*, 23–28.

Obenchain, V., Lawrence, M., Carey, V., Gogarten, S., Shannon, P., and Morgan, M. (2014). VariantAnnotation: a Bioconductor package for exploration and annotation of genetic variants. Bioinformatics *30*, 2076–2078.

Paik, D.Y., Janzen, D.M., Schafenacker, A.M., Velasco, V.S., Shung, M.S., Cheng, D., Huang, J., Witte, O.N., and Memarzadeh, S. (2012). Stem-like epithelial cells are concentrated in the distal end of the fallopian tube: a site for injury and serous cancer initiation. Stem Cells *30*, 2487–2497.

Patel, A.P., Tirosh, I., Trombetta, J.J., Shalek, A.K., Gillespie, S.M., Wakimoto, H., Cahill, D.P., Nahed, B.V., Curry, W.T., Martuza, R.L., et al. (2014). Single-cell RNA-seq highlights intratumoral heterogeneity in primary glioblastoma. Science *344*, 1396–1401.

Perets, R., Wyant, G.A., Muto, K.W., Bijron, J.G., Poole, B.B., Chin, K.T., Chen, J.Y.H., Ohman, A.W., Stepule, C.D., Kwak, S., et al. (2013). Transformation of the fallopian tube secretory epithelium leads to high-grade serous ovarian cancer in Brca;Tp53;Pten models. Cancer Cell *24*, 751–765.

Peters, W.M. (1986). Nature of "basal" and “reserve” cells in oviductal and cervical epithelium in man. Journal of Clinical Pathology *39*, 306–312.

Phipson, B., Lee, S., Majewski, I.J., Alexander, W.S., and Smyth, G.K. (2016). Robust hyperparameter estimation protects against hypervariable genes and improves power to detect differential expression. Ann Appl Stat *10*, 946–963.

Picelli, S., Faridani, O.R., Björklund, Å.K., Winberg, G., Sagasser, S., and Sandberg, R. (2014). Full-length RNA-seq from single cells using Smart-seq2. Nature Protocols *9*, 171–181.

Pils, D., Hager, G., Tong, D., Aust, S., Heinze, G., Kohl, M., Schuster, E., Wolf, A., Sehouli, J., Braicu, I., et al. (2012). Validating the impact of a molecular subtype in ovarian cancer on outcomes: a study of the OVCAD Consortium. Cancer Sci. *103*, 1334–1341.

Pisco, A.O., Brock, A., Zhou, J., Moor, A., Mojtahedi, M., Jackson, D., and Huang, S. (2013). Non-Darwinian dynamics in therapy-induced cancer drug resistance. Nat Commun *4*, 2467.

Quinlan, A.R., and Hall, I.M. (2010). BEDTools: a flexible suite of utilities for comparing genomic features. Bioinformatics *26*, 841–842.

Rimmer, A., Phan, H., Mathieson, I., Iqbal, Z., Twigg, S.R.F., WGS500 Consortium, Wilkie, A.O.M., McVean, G., and Lunter, G. (2014). Integrating mapping-, assembly- and haplotype-based approaches for calling variants in clinical sequencing applications. Nat Genet *46*, 912–918.

Ritchie, M.E., Phipson, B., Wu, D., Hu, Y., Law, C.W., Shi, W., and Smyth, G.K. (2015). limma powers differential expression analyses for RNA-sequencing and microarray studies. Nucleic Acids Research *43*, –e47.

Satija, R., Farrell, J.A., Gennert, D., Schier, A.F., and Regev, A. (2015). Spatial reconstruction of single-cell gene expression data. Nature Biotechnology *33*, 495–U206.

Schmidt, J.M., Panzilius, E., Bartsch, H.S., Irmler, M., Beckers, J., Kari, V., Linnemann, J.R., Dragoi, D., Hirschi, B., Kloos, U.J., et al. (2015). Stem-cell-like properties and epithelial plasticity arise as stable traits after transient Twist1 activation. Cell Rep *10*, 131–139.

Schwede, M., Waldron, L., Mok, S.C., Wei, W., Basunia, A., Merritt, M.A., Parmigiani, G., Harrington, D., Quackenbush, J., Birrer, M.J., et al. (2018). The impact of stroma on the discovery of molecular subtypes and prognostic gene signatures in serous ovarian cancer. bioRxiv *14*, 496406. https://www.biorxiv.org/content/10.1101/496406v1

Seirup, M., Chu, L.-F., Sengupta, S., Leng, N., Shafer, C.M., Duffin, B., Elwell, A.L., Bolin, J.M., Swanson, S., Stewart, R., et al. (2019). Tradeoff between more cells and higher read depth for single-cell RNA-seq spatial ordering analysis of the liver lobule. bioRxiv 764191. https://www.biorxiv.org/content/10.1101/764191v1

Singh, A., and Settleman, J. (2010). EMT, cancer stem cells and drug resistance: an emerging axis of evil in the war on cancer. Oncogene *29*, 4741–4751.

Soneson, C., and Robinson, M.D. (2018). Bias, robustness and scalability in single-cell differential expression analysis. Nat Meth *18*, 735–261.

Stuart, T., Butler, A., Hoffman, P., Hafemeister, C., Papalexi, E., Mauck, W.M., Hao, Y., Stoeckius, M., Smibert, P., and Satija, R. (2019). Comprehensive Integration of Single-Cell Data. Cell *177*, 1888–1902.e21.

Svensson, V., da Veiga Beltrame, E., and Pachter, L. (2019). Quantifying the tradeoff between sequencing depth and cell number in single-cell RNA-seq. bioRxiv 762773. https://www.biorxiv.org/content/10.1101/762773v1

Svensson, V., Vento-Tormo, R., and Teichmann, S.A. (2018). Exponential scaling of single-cell RNA-seq in the past decade. Nature Protocols *13*, 599–604.

Tan, T.Z., Miow, Q.H., Huang, R.Y.-J., Wong, M.K., Ye, J., Lau, J.A., Wu, M.C., Bin Abdul Hadi, L.H., Soong, R., Choolani, M., et al. (2013). Functional genomics identifies five distinct molecular subtypes with clinical relevance and pathways for growth control in epithelial ovarian cancer. EMBO Mol Med *5*, 1051–1066.

Tan, Y., Sinniah, R., Bay, B.H., and Singh, G. (1999). Metallothionein expression and nuclear size in benign, borderline, and malignant serous ovarian tumours. J. Pathol. *189*, 60–65.

Thomas, P.D. (2003). PANTHER: A Library of Protein Families and Subfamilies Indexed by Function. Genome Res. *13*, 2129–2141.

Topham, D.J., and Reilly, E.C. (2018). Tissue-Resident Memory CD8+ T Cells: From Phenotype to Function. Front Immunol *9*, 515.

Torre, L.A., Trabert, B., DeSantis, C.E., Miller, K.D., Samimi, G., Runowicz, C.D., Gaudet, M.M., Jemal, A., and Siegel, R.L. (2018). Ovarian cancer statistics, 2018. CA Cancer J Clin *68*, 284–296.

Tothill, R.W., Tinker, A.V., George, J., Brown, R., Fox, S.B., Lade, S., Johnson, D.S., Trivett, M.K., Etemadmoghadam, D., Locandro, B., et al. (2008). Novel molecular subtypes of serous and endometrioid ovarian cancer linked to clinical outcome. Clin. Cancer Res. *14*, 5198–5208.

van Deursen, J.M. (2014). The role of senescent cells in ageing. Nature *509*, 439–446.

Visvader, J.E. (2011). Cells of origin in cancer. Nature *469*, 314–322.

Wang, S., Chen, J.-Z., Zhang, Z., Huang, Q., Gu, S., Ying, K., Xie, Y., and Mao, Y. (2002). Cloning, characterization, and expression of calcyphosine 2, a novel human gene encoding an EF-hand Ca(2+)-binding protein. Biochem. Biophys. Res. Commun. *291*, 414–420.

Wang, Z.A., Mitrofanova, A., Bergren, S.K., Abate-Shen, C., Cardiff, R.D., Califano, A., and Shen, M.M. (2013). Lineage analysis of basal epithelial cells reveals their unexpected plasticity and supports a cell-of-origin model for prostate cancer heterogeneity. Nat. Cell Biol. *15*, 274–283.

Wu, R., Zhai, Y., Kuick, R., Karnezis, A.N., Garcia, P., Naseem, A., Hu, T.C., Fearon, E.R., and Cho, K.R. (2016). Impact of oviductal versus ovarian epithelial cell of origin on ovarian endometrioid carcinoma phenotype in the mouse. J. Pathol. *240*, 341–351.

Yang, J., Mani, S.A., Donaher, J.L., Ramaswamy, S., Itzykson, R.A., Come, C., Savagner, P., Gitelman, I., Richardson, A., and Weinberg, R.A. (2004). Twist, a master regulator of morphogenesis, plays an essential role in tumor metastasis. Cell *117*, 927–939.

Yin, X., Fang, S., Wang, M., Wang, Q., Fang, R., and Chen, J. (2016). EFEMP1 promotes ovarian cancer cell growth, invasion and metastasis via activated the AKT pathway. Oncotarget *7*, 47938–47953.

Yoshihara, K., Tajima, A., Yahata, T., Kodama, S., Fujiwara, H., Suzuki, M., Onishi, Y., Hatae, M., Sueyoshi, K., Fujiwara, H., et al. (2010). Gene expression profile for predicting survival in advanced-stage serous ovarian cancer across two independent datasets. PLoS ONE *5*, e9615.

Yoshihara, K., Tsunoda, T., Shigemizu, D., Fujiwara, H., Hatae, M., Fujiwara, H., Masuzaki, H., Katabuchi, H., Kawakami, Y., Okamoto, A., et al. (2012). High-risk ovarian cancer based on 126-gene expression signature is uniquely characterized by downregulation of antigen presentation pathway. Clin. Cancer Res. *18*, 1374–1385.

Zhang, Q., Wang, C., and Cliby, W.A. (2019a). Cancer-associated stroma significantly contributes to the mesenchymal subtype signature of serous ovarian cancer. Gynecol. Oncol. *152*, 368–374.

Zhang, S., Dolgalev, I., Zhang, T., Ran, H., Levine, D.A., and Neel, B.G. (2019b). Both fallopian tube and ovarian surface epithelium are cells-of-origin for high-grade serous ovarian carcinoma. Nat Commun *10*, 5367.

Ziegenhain, C., Vieth, B., Parekh, S., Reinius, B., Guillaumet-Adkins, A., Smets, M., Leonhardt, H., Heyn, H., Hellmann, I., and Enard, W. (2017). Comparative Analysis of Single-Cell RNA Sequencing Methods. Mol. Cell *65*, 631–643.e634.

Supplementary Information

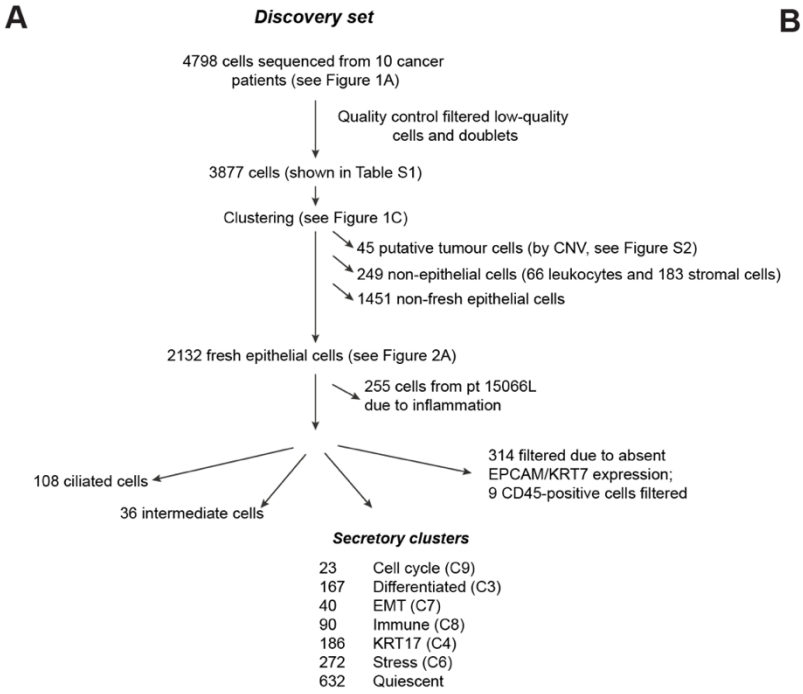

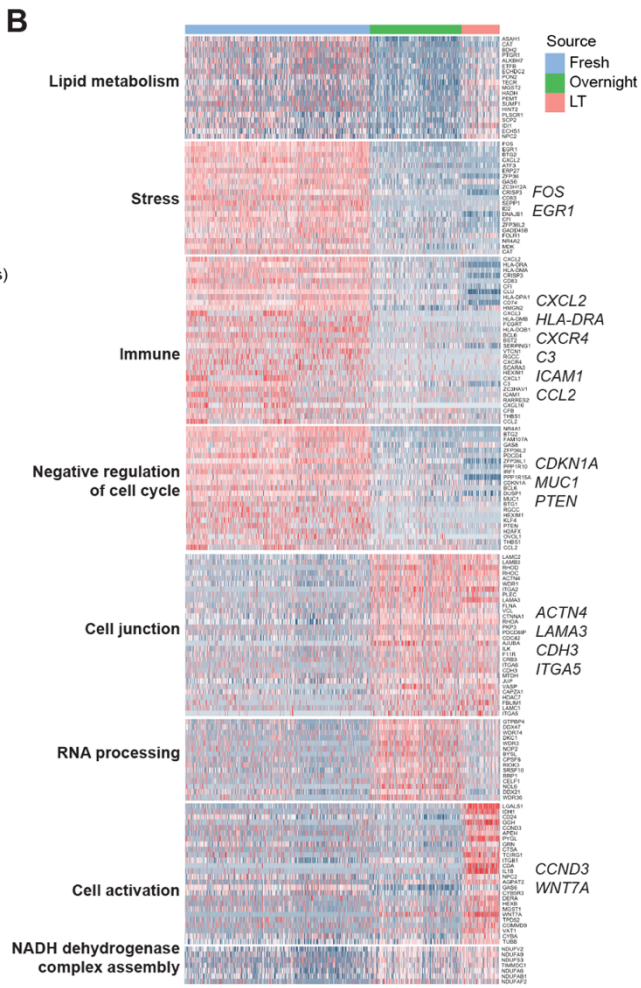

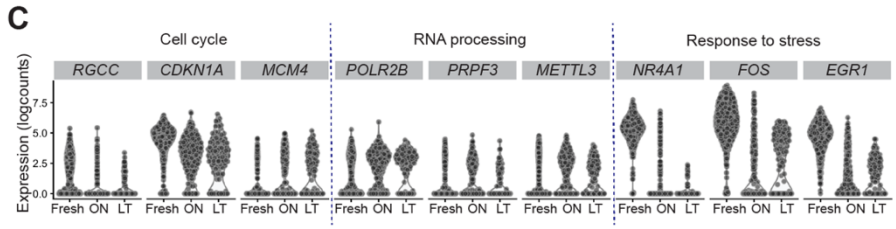

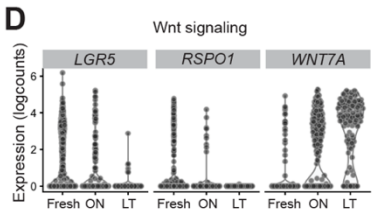

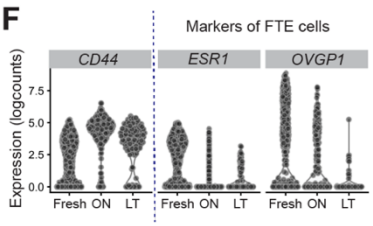

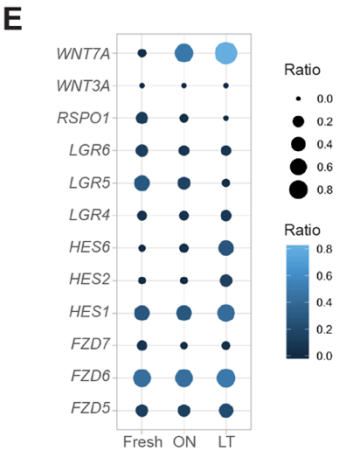

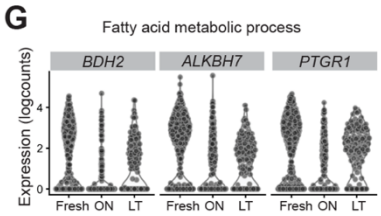

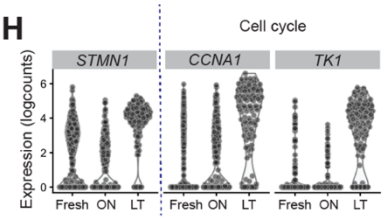

Figure S1, related to Figure 1. Landscape of single-cell transcriptomes in fallopian tube epithelium.

(A) Flowchart shows the process of cell filtering and analysis by using the cells from ten cancer patients.

(B) Heatmap shows the differences among fresh, overnight-cultured and long-term-cultured groups. Rows represent differentially expressed genes (fold-change > 2, FDR < 0.05) between the fresh and cultured cells. The genes are ordered by the gene ontology that they belong to. Columns represent single cells with the annotation bar that indicates the condition of each cell. LT, long-term.

(C) Violin plots show representative genes in three pathways (cell cycle, RNA processing and stress response) that are differentially expressed between fresh and overnight-cultured groups. FDR < 0.05, by limma voom. ON, overnight.

(D) Violin plots show the expression of representative genes (*LGR5*, *RSPO1* and *WNT7A*) in the Wnt signaling pathway that is dysregulated by the culturing conditions. FDR < 0.05, by limma voom.

(E) Dot plot shows that the Wnt and Notch signaling pathways are influenced by culture condition. The size and color of each dot represents the proportion of cells that express genes (rows) across three conditions (columns) as shown in the scales.

(F) Violin plots show the dysregulated expression of three genes (*CD44*, *ESR1* and *OVGP1*) after overnight culture. FDR < 0.05, by limma voom.

(G) Violin plots show that genes that are enriched in fatty acid processing are transiently switched off after overnight culturing. FDR < 0.05, by limma voom.

(H) Violin plots show that three genes (*STMN1*, *CCNA1* and *TK1*) related to the cell cycle pathway are significantly upregulated and expressed in most of cells after LT culturing. FDR < 0.05, by limma voom.

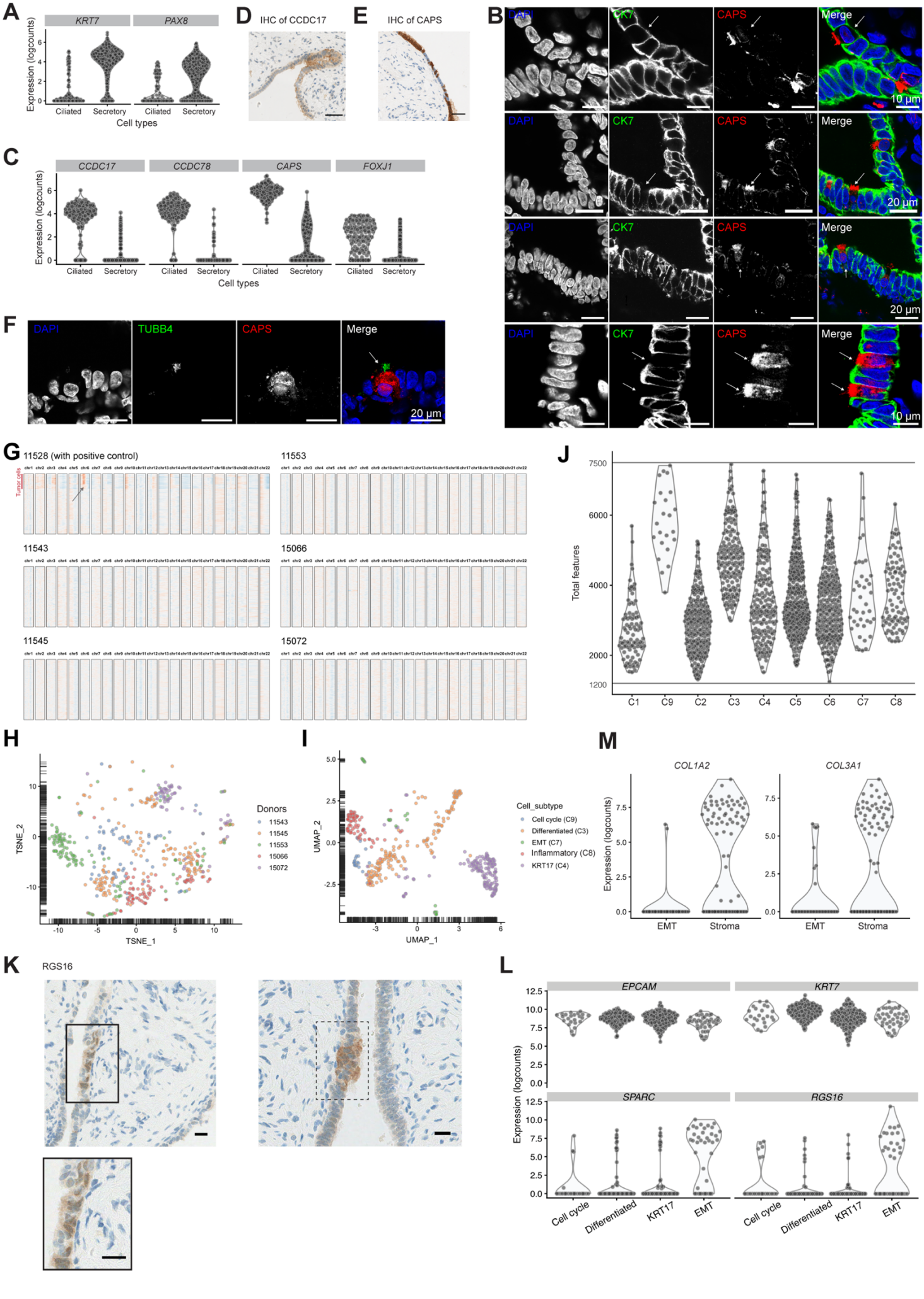
A
KRT7
PAX8
Expression (logcounts)
Ciliated
Secretory
Cell types
D
IHC of CCDC17
E
IHC of CAPS
B
DAPI
CK7
CAPS
Merge
10 μm
20 μm
C
CCDC17
CCDC78
CAPS
FOXJ1
F
TUBB4
G
11528 (with positive control)
11553
11543
15066
11545
15072
Tumor cells
J
Total features
C1
C9
C2
C3
C4
C5
C6
C7
C8
H
TSNE_1
TSNE_2
Donors
I
UMAP_1
UMAP_2
Cell_subtype
Cell cycle (C9)
Differentiated (C3)
EMT (C7)
Inflammatory (C8)
KRT17 (C4)
M
COL1A2
COL3A1
EMT
Stroma
K
RGS16
L
EPCAM
KRT7
SPARC
RGS16
Cell cycle
Differentiated
KRT17
EMT

Figure S2, related to Figure 2. Single-cell RNA sequencing of FTE cells identifies four novel secretory subtypes.

(A) Violin plots show the specific expression of secretory markers (*KRT7* and *PAX8*) in fresh secretory cells compared to fresh ciliated cells.

(B) IF staining of KRT7 and CAPS in the human FT, showing that KRT7 is a secretory marker and CAPS is a ciliated marker. Arrows indicate the examples of ciliated cells.

(C) Violin plots show the specific expression of ciliated marker genes (*CCDC17*, *CCDC78*, *CAPS* and *FOXJ1*) in fresh ciliated cells compared to fresh secretory cells.

(D) Immunohistochemistry (IHC) staining of a ciliated cell marker CCDC17 in the Formaldehyde Fixed-Paraffin Embedded (FFPE) human fallopian tube section. This CCDC17 antibody stained the cytoplasmic and membrane region of ciliated cells brown. Scale bar, 50 μm.

(E) IHC staining of a ciliated cell marker CAPS in the FFPE human fallopian tube section. The ciliated cells show strong brown staining of CAPS in the cytoplasm, which is absent in the secretory cells. Scale bar, 50 μm.

(F) IF staining shows an FTE ciliated cell (arrow) that was positive for both TUBB4 and CAPS positive in the human FT.

(G) Relative copy number variation inferred from the expression data. The arrow shows a small proportion of cells in patient 11528 that seemed to have copy number variation at Chr6. These cells also showed a somatic mutation of TP53 in the single-cell RNA-seq data, which is same as the one found in the tumor of patient 11528 (chr17: 7577515T>G). Each heatmap contains the cells from one patient. In the heatmap, each row is a single cell and columns represent the positions on chromosomes. Each block represents one chromosome in the order from Chr1 to Chr22. The color scale denotes the possibility of amplification or deletion. Red means amplification and blue means deletion as shown in the scale bar.

(H) *t*-SNE plot shows each secretory cluster consists of cells from multiple donors. Each point represents one cell that is colored by its donor as shown in the legend.

(I) UMAP plot shows the clusters within fresh secretory cells. Each point represents one cell that is colored by its cluster/subtype as shown in the legend.

(J) Violin plot shows that all cells that underwent the clustering analysis and passed the filter of doublets (number of genes detected ⩽ 7,500). The y-axis represents the total number of genes detected per cell. Each dot is one cell arranged by the cell subtypes (x-axis).

(K) IHC staining validates the EMT cluster with its marker, RGS16, in human FTE (dashed box). Scale bars, 20 μm.

(L) Violin plots showing that the EMT cluster of FTE cells has strong expression of *KRT7* and *EPCAM* as well as the upregulated expression of *SPARC* and *RGS16*.

(M) Violin plots show that two stromal markers were specifically expressed in mesenchymal cells but not in the EMT cluster of FTE secretory cells.

Table S5, related to Figure 2. Summary of the clustering results and annotations of secretory cells.

Clusters*	Name	Representative pathways	Marker genes
C1, C2, C5	Quiescent	-	-
C6	Stress	Response to stress	*FOS* and *JUN*
C9	Cell cycle	Cell cycle	*MCM2-7*, *MKI67*, *TK1* and *STMN1*
		DNA repair	*FANCD2*, *FANCI* and *MSH2*
		Chromatin remodeling	*HMGB2* and *SMC1A*
C3	Differentiated	RNA synthesis and transport	*PTBP1*, *ZNF259* and *PRPF38A*
C4	KRT17 cluster	MHC Class II	*HLA-DQA1*, *HLA-DPA1* and *HLA-DPB1*
		Cytokeratins	*KRT17* and *KRT23*
		Aldehyde dehydrogenases	*ALDH1A1* and *ALDH3B2*
			CDKN1A
C7	EMT		*RGS16*
		Extracellular matrix	*TIMP3* and *SPARC*

* The clusters were ordered by when it was described in the main text.

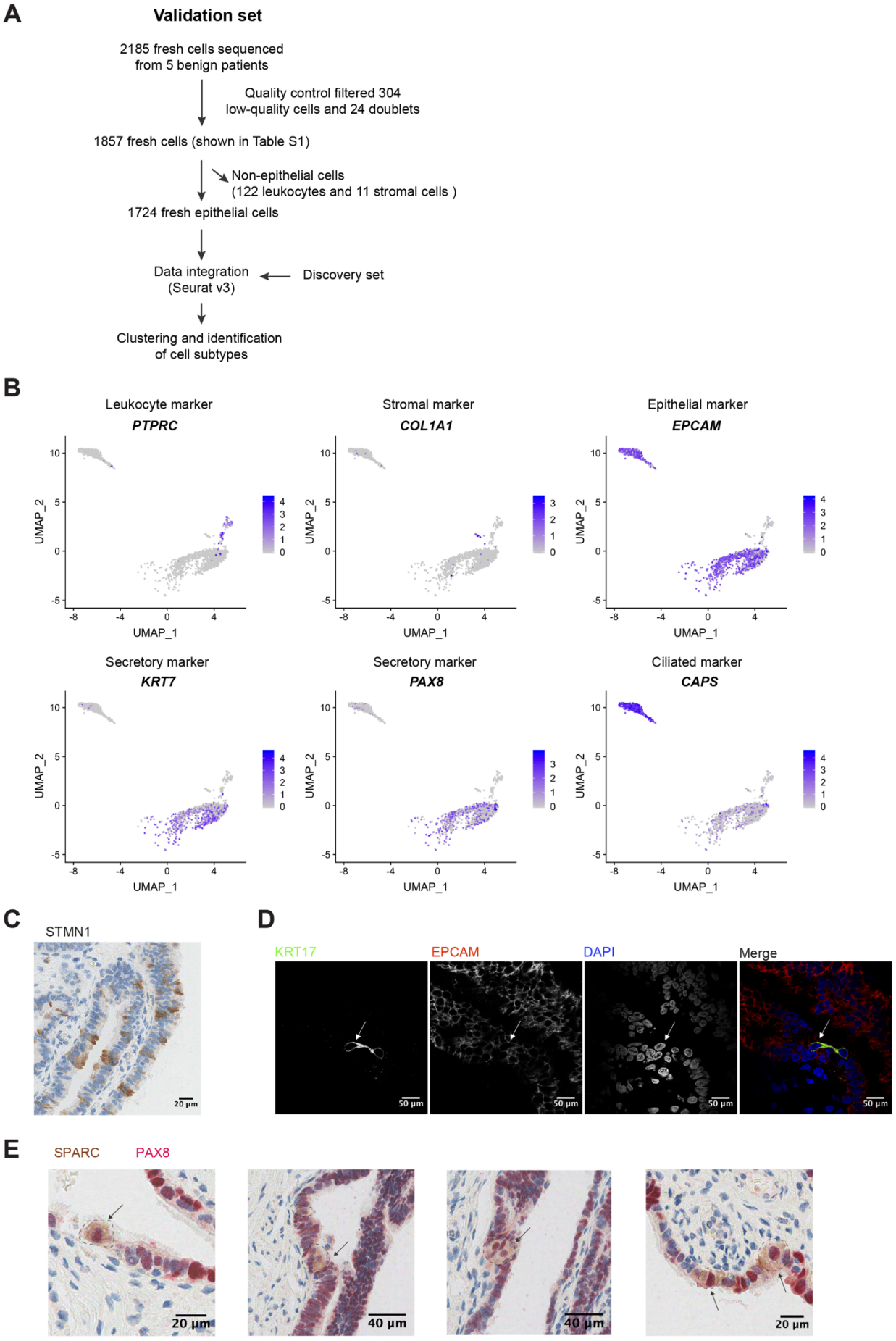
A
Validation set
2185 fresh cells sequenced from 5 benign patients
Quality control filtered 304 low-quality cells and 24 doublets
1857 fresh cells (shown in Table S1)
Non-epithelial cells (122 leukocytes and 11 stromal cells)
1724 fresh epithelial cells
Data integration (Seurat v3)
Discovery set
Clustering and identification of cell subtypes
B
Leukocyte marker
PTPRC
Stromal marker
COL1A1
Epithelial marker
EPCAM
Secretory marker
KRT7
Secretory marker
PAX8
Ciliated marker
CAPS
UMAP_1
UMAP_2
C
STMN1
20 μm
D
KRT17
EPCAM
DAPI
Merge
50 μm
E
SPARC
PAX8
20 μm
40 μm
40 μm
20 μm

Figure S3, related to Figure 3. Validation of the secretory subtypes in the FTE of benign donors by using scRNA-seq.

(A) Flowchart shows the processing of the validation set, in which we profiled 2185 single-cell transcriptomes from five benign patients. After the initial filtering, 1875 cells were left as shown in Figure 3A. By using the data integration, we removed the batch effects between the discovery set and the validation set and then merged the two datasets. We next clustered the merged datasets to identify the four secretory subtypes in the FTE secretory cells from benign patients.

(B) Scatter plots show the expression of marker genes in the FT cells from five benign patients. The x- and y-axes represent the first two components of the UMAP analysis. Each dot (cell) is colored by the expression level of the marker gene (subtitle). The result shows the $CD45^{+}$ leukocytes, $COL1A1^{+}$ stromal cells, $KRT7^{+}$ $PAX8^{+}$ $EPCAM^{+}$ secretory cells and $CAPS^{+}$ $EPCAM^{+}$ ciliated cells.

(C) IHC shows the STMN1 positive cell cycle subtype in the FTE of a benign patient.

(D) IF staining shows a KRT17 and EPCAM double positive cell (KRT17 subtype) in the FTE of a benign patient.

(E) IHC images show the SPARC and PAX8 double positive cells in the FTE in the FTE of multiple benign patients (arrows and dashed circles).

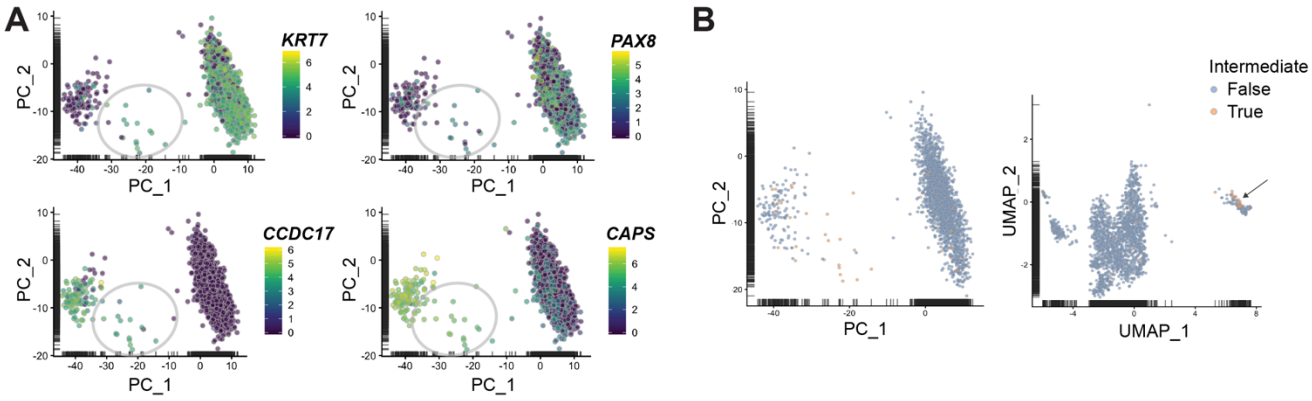

Figure S4, related to Figure 4. Non-traditional cell subtypes in the fallopian tube epithelial layer.

(A) PCA plots show that the intermediate cell population (grey circles) has the expression of both secretory markers (*KRT7* and *PAX8*) and ciliated markers (*CCDC17* and *CAPS*).

(B) Scatter plots highlight the position of intermediate population. The cells are colored by whether they belong to the intermediate population or not as shown in the legend. The arrow indicates the intermediate population that is close to the ciliated cells in the two-dimensional space computed by UMAP.

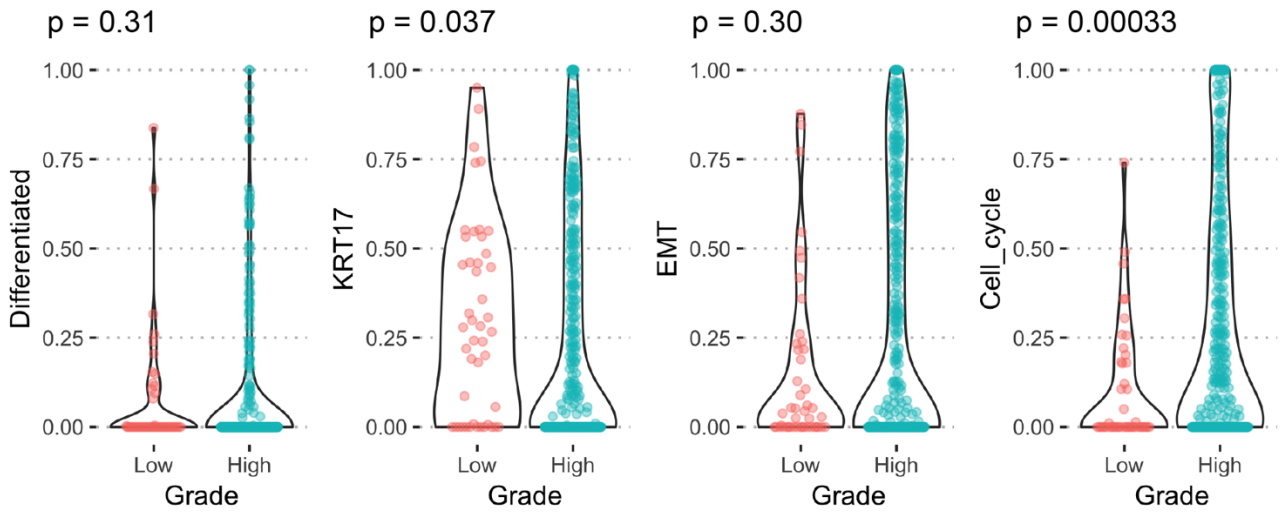

Figure S5, related to Figure 5. The repertoire of phenotypic heterogeneity of serous ovarian cancer revealed by deconvolution analysis.

Violin plots visualize the different composition of cell states between low-grade and high-grade serous ovarian cancer in the AOCS dataset and GSE1726. The p values were calculated by the Wilcoxon test between the low-grade and high-grade tumors.

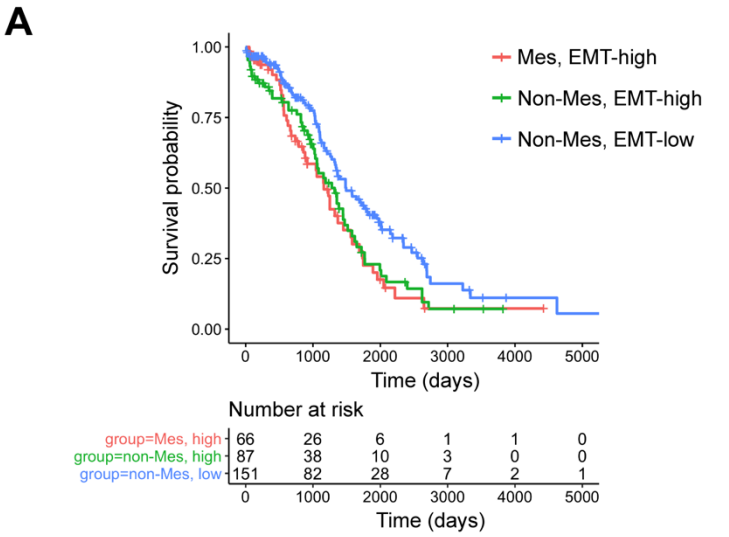
A
Survival probability
1.00
0.75
0.50
0.25
0.00
Mes, EMT-high
Non-Mes, EMT-high
Non-Mes, EMT-low
0
1000
2000
3000
4000
5000
Time (days)
Number at risk
group=Mes, high 66 26 6 1 1 0
group=non-Mes, high 87 38 10 3 0 0
group=non-Mes, low 151 82 28 7 2 1
0
1000
2000
3000
4000
5000
Time (days)

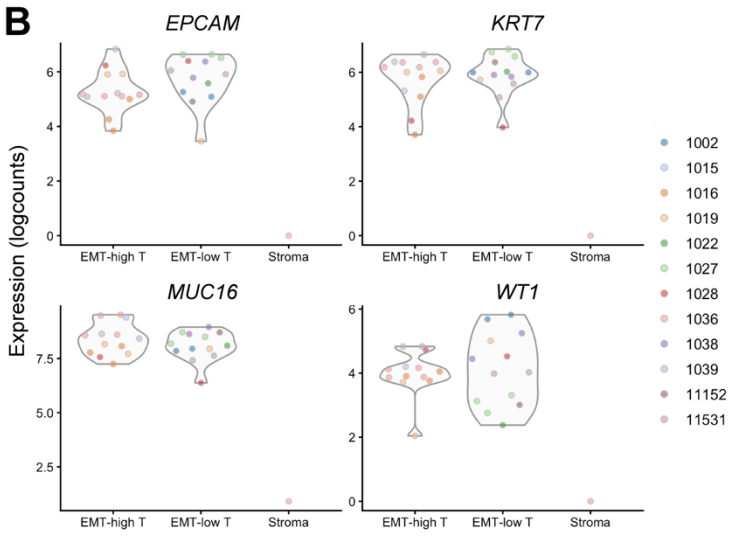
B
EPCAM
KRT7
MUC16
WT1
Expression (logcounts)
EMT-high T
EMT-low T
Stroma
1002
1015
1016
1019
1022
1027
1028
1036
1038
1039
11152
11531

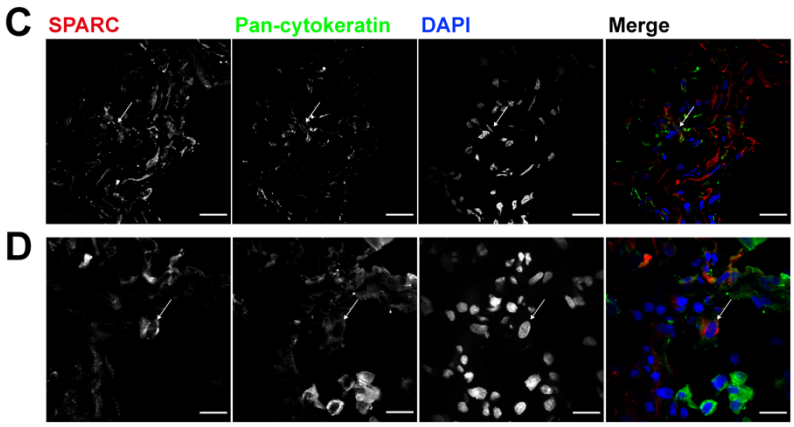
C
SPARC
Pan-cytokeratin
DAPI
Merge
D

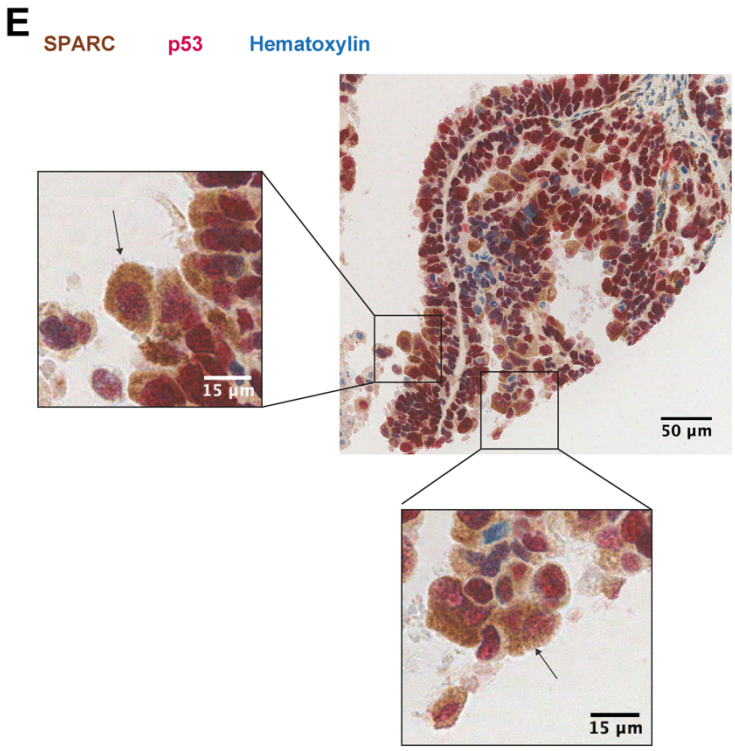
E
SPARC
p53
Hematoxylin
15 µm
50 µm
15 µm

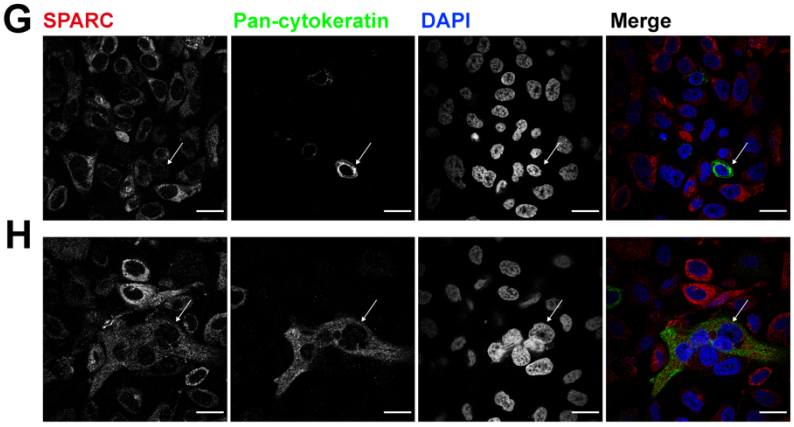
G
SPARC
Pan-cytokeratin
DAPI
Merge
H

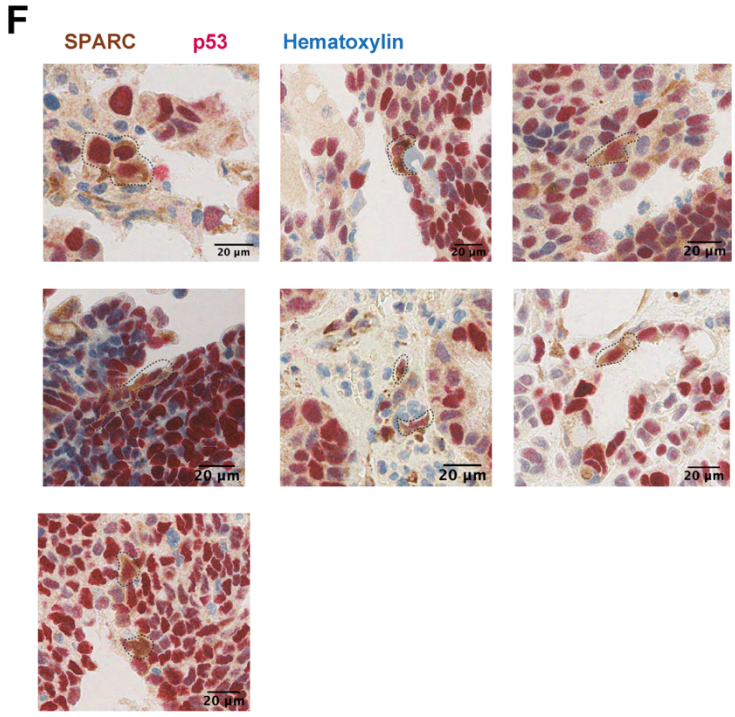
F
SPARC
p53
Hematoxylin
20 µm

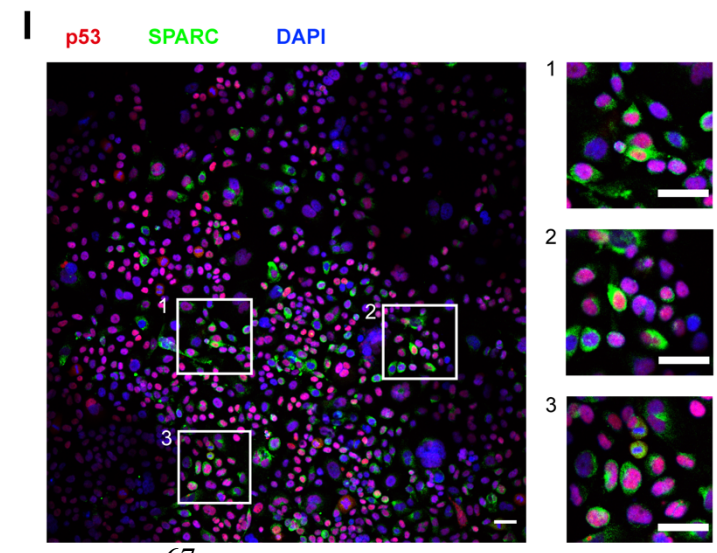
I
p53
SPARC
DAPI
1
2
3

Figure S6, related to Figure 6. Mesenchymal-like tumor cells in pre-chemotherapy tumors and KURAMOCHI cell line.

(A) Kaplan-Meier curves compare the overall survival of three groups of patients, namely EMT-high mesenchymal (EMT-high, Mes), EMT-high non-mesenchymal (EMT-high, non-Mes) and EMT-low non-mesenchymal (EMT-low, non-Mes). The result showed that the prognosis of the EMT-high non-Mes tumors was close to EMT-high Mes tumors, and worse than that of the EMT-low non-Mes tumors. By using the two-variate proportion hazards regression model, the hazard ratio of the EMT-high group was 1.51 (95% CI: 1.07-2.13, p = 0.018), and the hazard ratio of the mesenchymal group was 1.10 (95% CI: 0.74-1.64, p = 0.63). There were three EMT-low mesenchymal samples, which were excluded from the analysis due to the small group size. In the figure, the x-axis represents the time (days), and the y-axis represents the survival probability. Each short vertical line indicates a censoring event. In the table, each entry denotes the number of survived cases at each time point (column) for each group of patients (row).

(B) Expression levels of ovarian cancer markers (*EPCAM*, *KRT7*, *MUC16* and *WT1*) were significantly higher in both EMT-high and EMT-low tumor samples compared to stromal samples in which these markers showed almost no expression.

(C) IF staining shows a SPARC and pan-cytokeratin double positive cell (arrow). Scale bars, 20 μm.

(D) IF staining shows a SPARC positive and pan-cytokeratin negative population with similar nuclear sizes as tumor cells. Scale bars, 20 μm.

(E) IHC shows the expression of SPARC in p53-expressing HGSOC cells (arrows). The p53 antibody stained the nuclei pink and the SPARC antibody stained the cytoplasm brown. The two small subfigures are the zoomed-in images of the larger subfigure on the right top.

(F) IHC shows more examples of SPARC and p53 double positive cancer cells from six serous ovarian cancer patients (dashed circles).

(G) KURAMOCHI cells exhibited two phenotypes, a SAPRC positive mesenchymal-like phenotype and a pan-cytokeratin positive epithelial phenotype (arrow). Scale bars, 20 μm.

(H) A SPARC and pan-cytokeratin double positive population also exists in KURAMOCHI cells (arrow). Scale bars, 20 μm.

(I) IF images show that SPARC was expressed in the p53-expressing KURAMOCHI cells. We zoomed into three regions (white boxes, numbered) as shown in the three small subfigures on the right side. Scale bars, 20 μm.

Table S9, related to Table 1. Full results of survival analysis for TCGA, AOCS and CuratedOvarianData.

TCGA	**n = 305, number of events = 183**			
	Hazard ratio	Lower 95% CI	Upper 95% CI	p value
EMT score	2.124	1.184	3.812	0.0116
Stage (late vs early)	1.671	0.779	3.585	0.1871

AOCS	**n = 253, number of events = 109**			
	Hazard ratio	Lower 95% CI	Upper 95% CI	p value
EMT score	2.110	1.214	3.666	0.0081
Stage (late vs early)	3.880	1.180	12.756	0.0255
Grade (high vs low)	1.598	0.488	5.238	0.4386

E.MTAB.386	**n = 128, number of events = 73**			
	Hazard ratio	Lower 95% CI	Upper 95% CI	p value
EMT score	3.107	1.214	7.953	0.0181

GSE13876	**n = 144, number of events = 105**			
	Hazard ratio	Lower 95% CI	Upper 95% CI	p value
EMT score	2.958	1.282	6.826	0.0110
Grade (high vs low)	1.136	0.763	1.690	0.5290

GSE26193	**n = 79, number of events = 60**			
	Hazard ratio	Lower 95% CI	Upper 95% CI	p value
EMT score	2.582	1.038	6.421	0.0413
Grade (low vs high)	1.760	0.989	3.130	0.0546
Stage (late vs early)	2.949	1.349	6.444	0.0067

GSE26712	**n = 185, number of events = 129**			
	Hazard ratio	Lower 95% CI	Upper 95% CI	p value
EMT score	2.0345	1.065	3.886	0.0315

GSE32062.GPL6480	**n = 260, number of events = 121**			
	Hazard ratio	Lower 95% CI	Upper 95% CI	p value
EMT score	1.886	0.987	3.603	0.0547
Grade (low vs high)	1.040	0.726	1.487	0.8322

GSE49997	**n = 170, number of events = 47**

	Hazard ratio	Lower 95% CI	Upper 95% CI	p value
EMT score	2.825	1.159	6.884	0.0223
Grade (high vs low)	3.451	1.450	8.210	0.0051
Stage (early vs late)	1.876	0.440	8.000	0.3955

GSE51088	**n = 113, number of events = 93**			
	Hazard ratio	Lower 95% CI	Upper 95% CI	p value
EMT score	2.0874	1.1126	3.916	0.0219
Grade (low vs high)	1.2295	0.6338	2.385	0.5411
Stage (late vs early)	1.5325	0.5531	4.246	0.4117